



A nanomaterial targeting the spike protein captures SARS-CoV-2 variants and promotes viral elimination

Guofang Zhang^{1,16}, Yalin Cong^{1b,2,3,4,16}, Feng-Liang Liu^{1b,5,16}, Jiufeng Sun^{6,16}, Jiantian Zhang⁷, Guoli Cao^{1,8,9}, Lingqiang Zhou¹⁰, Wenjie Yang^{1,8}, Qingle Song^{1,8}, Fangjun Wang¹⁰, Ke Liu¹, Jing Qu¹, Jing Wang³, Min He¹⁰, Shun Feng¹⁰, Didar Baimanov^{1b,2,4,11}, Wei Xu^{1b,2,4,11}, Rong-Hua Luo⁵, Xin-Yan Long⁵, Shumin Liao¹², Yunping Fan¹², Yu-Feng Li^{1b,2,4,11}, Bai Li^{2,11}, Ximing Shao¹, Guocheng Wang¹, Lijing Fang¹, Huaiyu Wang¹, Xue-Feng Yu^{1b}, Yan-Zhong Chang^{1b,9}, Yuliang Zhao^{1b,2,4,13,14}, Liang Li¹, Peng Yu⁷, Yong-Tang Zheng^{1b,5}✉, Diana Boraschi^{1,8,15}, Hongchang Li^{1b}✉, Chunying Chen^{1b,2,4,13,14}✉, Liming Wang^{1b,2,3,4,11}✉ and Yang Li^{1b,8}✉

The global emergency caused by the severe acute respiratory syndrome coronavirus 2 (SARS-CoV-2) pandemic can only be solved with effective and widespread preventive and therapeutic strategies, and both are still insufficient. Here, we describe an ultrathin two-dimensional CuInP₂S₆ (CIPS) nanosheet as a new agent against SARS-CoV-2 infection. CIPS exhibits an extremely high and selective binding capacity (dissociation constant (K_D) < 1 pM) for the receptor binding domain of the spike protein of wild-type SARS-CoV-2 and its variants of concern, including Delta and Omicron, inhibiting virus entry and infection in angiotensin converting enzyme 2 (ACE2)-bearing cells, human airway epithelial organoids and human ACE2-transgenic mice. On association with CIPS, the virus is quickly phagocytosed and eliminated by macrophages, suggesting that CIPS could be successfully used to capture and facilitate virus elimination by the host. Thus, we propose CIPS as a promising nanodrug for future safe and effective anti-SARS-CoV-2 therapy, and as a decontamination agent and surface-coating material to reduce SARS-CoV-2 infectivity.

The corona virus disease 2019 (COVID-19), induced by the severe acute respiratory syndrome coronavirus 2 (SARS-CoV-2), broke out in December 2019 and has led to a worldwide health crisis¹. The US Food and Drug Administration granted remdesivir, hydroxychloroquine, Paxlovid and molnupiravir Emergency Use Authorization to treat COVID-19^{2–6}, but revoked the use of hydroxychloroquine due to its lack of effectiveness in clinical use^{7–10}, while the interim results of the World Health Organization's Solidarity trial with remdesivir showed no substantial effect^{11–13}. Several mutations in the virus spike (S)

protein have generated variants with increased infectivity¹⁴. The rapid spreading of SARS-CoV-2 variants of concern (VOCs) has shown substantial limitations in the effectiveness of the currently approved anti-SARS-CoV-2 drugs, neutralizing antibodies and vaccines^{15,16}. Despite considerable efforts to repurpose drugs^{17,18}, novel compounds with effective antiviral activity are still required for the treatment and containment of SARS-CoV-2 infection¹⁹.

Infection by SARS-CoV-2 requires the binding of the receptor binding domain (RBD) of the S protein of SARS-CoV-2 to the host's cellular angiotensin converting enzyme 2 (ACE2) receptor²⁰.

¹Shenzhen Institute of Advanced Technology, Chinese Academy of Sciences, Shenzhen, China. ²CAS Key Laboratory for Biomedical Effects of Nanomaterials and Nanosafety, CAS Center for Excellence in Nanoscience, Institute of High Energy Physics and National Center for Nanoscience and Technology of China, Chinese Academy of Sciences, Beijing, China. ³State Key Laboratory of Natural and Biomimetic Drugs, School of Pharmaceutical Sciences, Peking University, Beijing, China. ⁴University of the Chinese Academy of Science, Beijing, China. ⁵Key Laboratory of Animal Models and Human Disease Mechanisms of the Chinese Academy of Sciences, Key Laboratory of Bioactive Peptides of Yunnan Province, KIZ-CUHK Joint Laboratory of Bioresources and Molecular Research in Common Diseases, Kunming Institute of Zoology, Chinese Academy of Sciences, Kunming, China. ⁶Guangdong Provincial Institute of Public Health, Guangdong Provincial Center for Disease Control and Prevention, Guangzhou, China. ⁷State Key Laboratory of Optoelectronic Materials and Technologies, Guangzhou Key Laboratory of Flexible Electronic Materials and Wearable Devices, Nanotechnology Research Center, School of Materials Science and Engineering, Sun Yat-sen University, Guangzhou, China. ⁸Laboratory of Immunology and Nanomedicine, and China-Italy Joint Laboratory of Pharmacobiotechnology for Medical Immunomodulation, Shenzhen Institute of Advanced Technology, Chinese Academy of Sciences, Shenzhen, China. ⁹Laboratory of Molecular Iron Metabolism, College of Life Science, Hebei Normal University, Shijiazhuang, China. ¹⁰CAS Key Laboratory of Separation Sciences for Analytical Chemistry, Dalian Institute of Chemical Physics, Chinese Academy of Sciences, Dalian, China. ¹¹CAS-HKU Joint Laboratory of Metallomics on Health and Environment, and National Consortium for Excellence in Metallomics, Institute of High Energy Physics, Chinese Academy of Sciences, Beijing, China. ¹²Department of Otolaryngology, The Seventh Affiliated Hospital of Sun Yat-sen University, Shenzhen, China. ¹³The GBA National Institute for Nanotechnology Innovation, Guangzhou, China. ¹⁴Research Unit of Nanoscience and Technology, Chinese Academy of Medical Sciences, Beijing, China. ¹⁵Institute of Biochemistry and Cell Biology, National Research Council, Napoli, Italy. ¹⁶These authors contributed equally: Guofang Zhang, Yalin Cong, Feng-Liang Liu, Jiufeng Sun. ✉e-mail: zhengyt@mail.kiz.ac.cn; hc.li@siat.ac.cn; chenchy@nanocr.cn; wangliming@ihep.ac.cn; yang.li@siat.ac.cn

Anti-SARS-CoV-2 neutralizing monoclonal antibodies (mAbs) have been designed for targeted interaction with the RBD of the S protein^{21,22} or the epitopes of the RBD-ACE2 binding site^{23–25}, or selected for potent neutralization activity^{26–28}. In addition to logistic hurdles (high dosage of 4–100 mg per kg body weight for effective therapy, complex storage and shipping conditions), an important drawback of the use of mAbs is their scarce efficacy against the SARS-CoV-2 variants²⁹, especially evident for the Omicron VOC^{15,16}.

Searching for alternative tools with less specificity and therefore with a broader therapeutic capacity, the antimicrobial and antiviral capacity of nanomaterials (NMs)^{30,31} has raised particular interest. VivaGel, a well-known antiviral dendrimer gel, has been used for human immunodeficiency virus and herpes simplex virus prevention by blocking the virus–cell interaction³². Metal NMs display antiviral capacity through the interaction of the metallic atoms with virus components, as in the cases of silver³³ and gold³⁴ NMs. Gold NMs, with a tunable surface chemistry design that mimics virus-adhesive heparan sulfate, have been successfully applied to inhibit infection by various viruses³¹. Owing to its β -sheet planar structure and positive surface charges^{35–37}, the RBD is preferentially adsorbed on two-dimensional (2D) NM surfaces with abundant negative charges, which led us to screen a series of negatively charged NMs for antiviral activity (Extended Data Fig. 1 and Supplementary Figs. 1 and 2). We have identified copper indium thiophosphate (CuInP₂S₆, denoted CIPS) nanosheets (NSs), an ultrathin 2D NM, for its powerful anti-SARS-CoV-2 capacity.

CIPS inhibits SARS-CoV-2 infection in vitro and in vivo

CIPS NSs were exfoliated from the bulk CIPS (Supplementary Fig. 3a) by Li intercalation. The crystalline nature of CIPS was proven by X-ray diffraction (Supplementary Fig. 3b). The exfoliated CIPS showed a structure of a few layers with a mean size of ~200 nm, determined by scanning electron microscopy (Supplementary Fig. 3c) and transmission electron microscopy (TEM; Fig. 1a), and an average thickness of ~3.1 nm, determined by atomic force microscopy (AFM; Fig. 1b,c). According to extended X-ray absorption fine structure (EXAFS) analysis, the copper atoms are coordinated to sulfur atoms (Fig. 1d, Supplementary Fig. 3d–g and Supplementary Table 1), with a majority of the Cu atoms having a valence of +1 (Supplementary Table 2). Sulfur is present as sulfide (S²⁻) with a valence of –2 (Supplementary Fig. 3h,i). According to In L₃-edge X-ray absorption near-edge spectroscopy (XANES), In mainly forms In–S, In–P and In–O bonds, and exhibits a valence of +3 (Supplementary Fig. 3j). The chemical form of In is consistent with

the crystal structure of CIPS, in which the In atoms lie between two different CIPS surfaces and stably support the structure of CIPS by coordinating with the P and S atoms (Fig. 1e). The crystal structure of CIPS is presented in the schematic diagrams in Fig. 1e, which show the Cu, S and P atoms mainly localized on the surface and the In atoms immersed in the NS.

The antiviral effect of CIPS was investigated with the established SARS-CoV-2 pseudovirus (SC2-P, expressing the SARS-CoV-2 S protein) and the SARS pseudovirus (SARS-P, expressing the SARS S protein; Supplementary Fig. 1). CIPS showed excellent biocompatibility with several human and monkey epithelial and myeloid cell lines (Supplementary Fig. 4). The capacity of CIPS to inhibit SC2-P infection was dose-dependent, as shown by a luciferase reporter assay on both Vero-E6 and human embryonic kidney 293T cells stably transfected with hACE2 (ACE2/293T) cells (Extended Data Fig. 2a) and by immunofluorescence in transiently transfected ACE2-overexpressing 293T cells (ACE2-OE) cells (Extended Data Fig. 2b, and for a quantitative evaluation see Extended Data Fig. 2c). The CIPS inhibitory effect was evident at early time points (0.5–2 h; Extended Data Fig. 2d,e) and persisted up to 15 h (Supplementary Fig. 5). Although we could detect many SC2-P particles around cells at 15 h (Supplementary Fig. 5a–c), the virus apparently could not enter and infect cells, as indicated by the luciferase activity (Supplementary Fig. 5d).

We further assessed the antiviral effects of CIPS with the authentic SARS-CoV-2 virus. Forty-eight hours after SARS-CoV-2 infection of Vero-E6 cells in the presence of CIPS, the SARS-CoV-2 infection rate had decreased in a CIPS dose-dependent fashion (Fig. 1f,g and Supplementary Fig. 6), whereas cell viability was not affected, with an excellent selectivity index (SI, the ratio between cytotoxic and antiviral concentrations) exceeding 17.6 (Fig. 1g). The phase-contrast images in Fig. 1h also show that CIPS inhibited the virus-induced cytopathic effect. The antiviral effect of CIPS was also evident when SARS-CoV-2-infected Vero-E6 cells were treated with CIPS post-infection (Fig. 1i,j): CIPS still effectively inhibited SARS-CoV-2 in vitro when added 24 h after infection, with maximal viral inhibition at 4 h from infection.

The anti-SARS-CoV-2 effect of CIPS was also assessed using air/liquid interface-cultured human airway epithelial organoids (Fig. 1k–n). The organoids presented a multilayer airway epithelial structure with ciliated cells on the air-facing side, closely mimicking the structure of the human respiratory tract, which makes them a realistic model for human respiratory infection. CIPS treatment induced a 40% decrease in SARS-CoV-2 replication (Fig. 1k), together with effective protection of tissue integrity,

Fig. 1 | Characterization of CIPS and its anti-SARS-CoV-2 capacity in vitro. **a**, TEM image of exfoliated a CIPS NS. **b,c**, AFM image (**b**) and measurement (**c**) of CIPS NSs, showing the thickness (colour code bar) and size (green line, 280 nm) distribution (**c** represents the thickness of the area, depicted by the green line in **b**). **d**, Coordination structure of Cu with S atoms in CIPS, determined by EXAFS. **e**, Schematic illustration of the CIPS crystal structure from the top (y - x), lateral (z - y) and front (z - x) sides. **f**, Schematic representation of the CIPS capacity to inhibit SARS-CoV-2 infection of target cells. **g**, Anti-SARS-CoV-2 effect and cytotoxicity of CIPS towards Vero-E6 cells in vitro. IC₅₀, 50% inhibitory/cytotoxic concentration (pM); EC₅₀, 50% effective/antiviral concentration (pM); SI, ratio between IS₅₀ and EC₅₀. Mean \pm s.e.m. of $n = 3$ –5 biological replicates. **h**, Phase-contrast images of Vero-E6 cells 48 h post-infection with SARS-CoV-2 in the absence or presence of CIPS. The numbers at the bottom of the images represent the percentage of the cell culture surface covered by cells, which correlates with cell survival. Scale bars, 50 μ m. **i**, Antiviral effect of post-infection treatment of Vero-E6 cells with CIPS. Cells were infected with SARS-CoV-2 for 2 h and then treated with CIPS. The intracellular SARS-CoV-2 was evaluated after 48 h. Mean \pm s.e.m. of $n = 3$ biological replicates. **j**, Therapeutic antiviral effect of CIPS against SARS-CoV-2. Vero-E6 cells were infected with SARS-CoV-2, and CIPS was added at various times after virus infection. Mature SARS-CoV-2 released into the medium was measured after 48 h. Mean \pm s.e.m. of $n = 5$ biological replicates. **k–n**, Anti-SARS-CoV-2 capacity of CIPS in human airway epithelial organoids: SARS-CoV-2 replication was evaluated in organoids infected with the virus in the absence or presence of CIPS (**k**), images of haematoxylin and eosin (H&E) staining of cultured tissue cross-sections (**l**), confocal microscopy images of human airway epithelial organoids after SARS-CoV-2 infection in the absence or presence of CIPS (the white arrows indicate tissue damage (**m**)) and the thickness of human respiratory epithelium sections measured by ImageJ (**n**). Scale bars, 20 μ m. Blank, uninfected tissue; virus, tissue infected with SARS-CoV-2; virus + CIPS, tissue infected with SARS-CoV-2 and treated with CIPS. DAPI, 4,6-diamidino-2-phenylindole. For the data in **k**, the mean \pm s.e.m. of $n = 3$ biological replicates is presented; for the data in **n**, the mean \pm s.e.m. of $n = 3$ technical replicates from a representative experiment out of two performed is shown. In **i,j,k** and **n**, the statistical significance was calculated by one-way analysis of variance (ANOVA) with Tukey's multiple comparisons test. Open circles represent the individual replicate values.

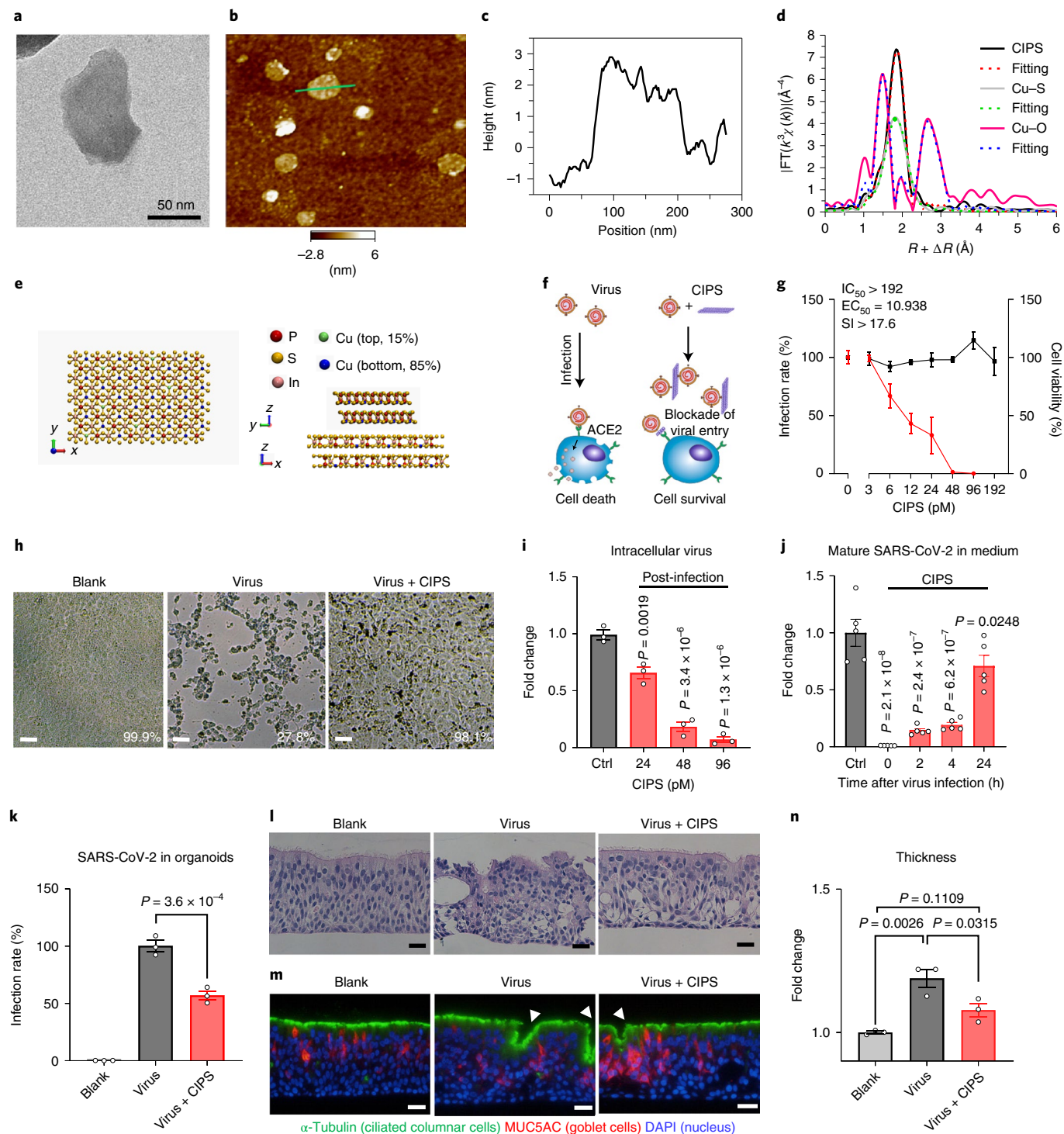
which was severely damaged by SARS-CoV-2 infection (Fig. 11,m). SARS-CoV-2 infection also caused an increase in the thickness of the epithelium, a sign of ongoing infection³⁸, which was reduced by CIPS treatment (Fig. 1n).

We further assessed the anti-SARS-CoV-2 capacity of CIPS in human ACE2 (hACE2) transgenic mice in vivo. Mice were treated with CIPS (4–8 mg per kg body weight) before or after intranasal infection with SARS-CoV-2 (Fig. 2a,b), and the presence of SARS-CoV-2 in the lung was evaluated 3 days post-infection. Infection was significantly decreased by treatment with both doses of CIPS (Fig. 2a), with CIPS being highly effective in both therapeutic

and prophylactic treatments (Fig. 2b). The reduction in infection was confirmed by reduced tissue injury and leukocyte infiltration (Fig. 2c), and by the decreased expression of inflammatory factors in the lung (Fig. 2d).

The mechanism of CIPS-dependent SARS-CoV-2 inhibition

After excluding possible metallic ion effects (Supplementary Fig. 7), we confirmed the interaction of CIPS with SC2-P by TEM (Supplementary Fig. 8a), variation in the physicochemical properties of CIPS (Supplementary Fig. 8b,c) and western blotting (Supplementary Fig. 8d). CIPS could effectively adsorb and



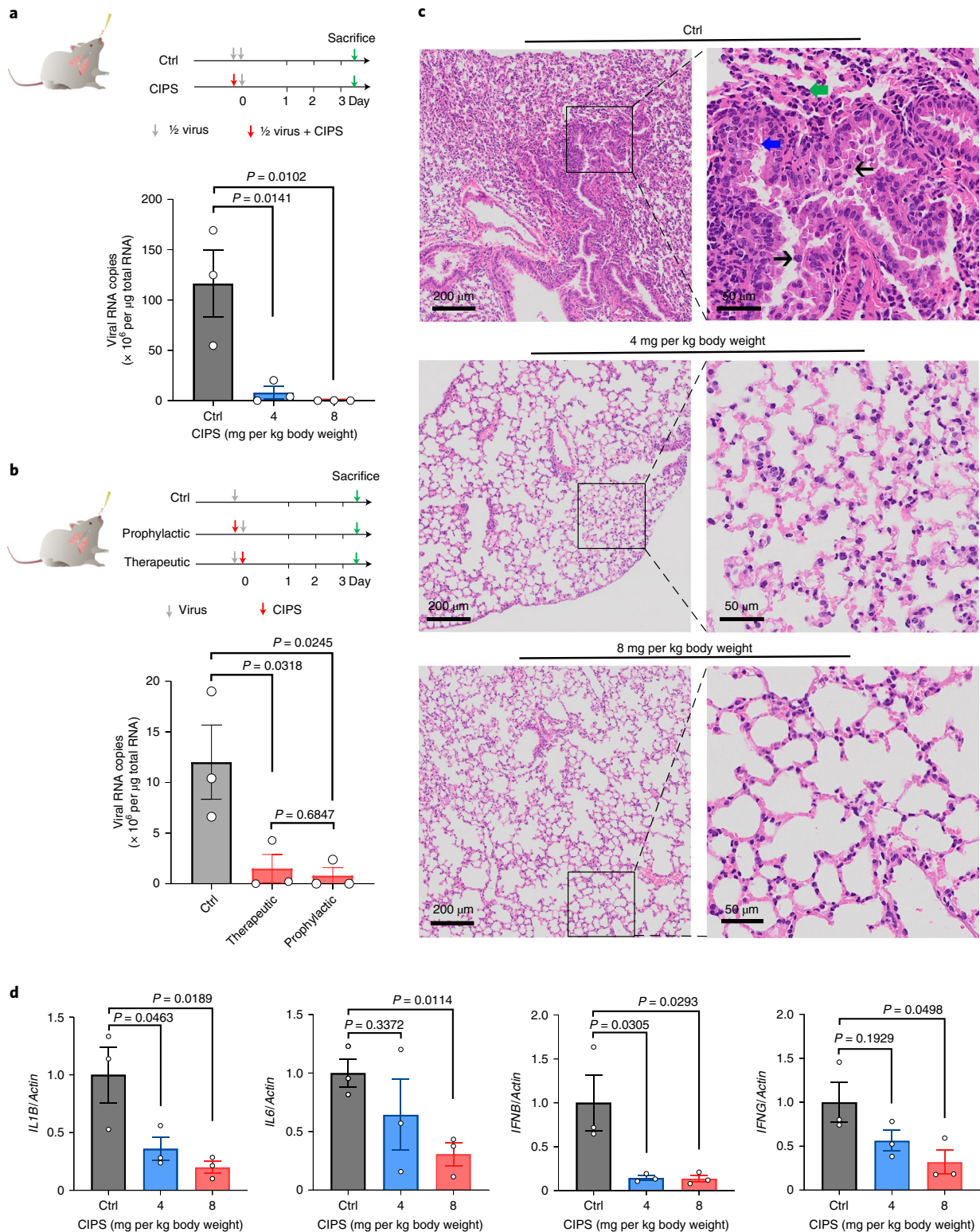


Fig. 2 | CIPS inhibits SARS-CoV-2 infection in hACE2 mice in vivo. **a, b**, Protocol for in vivo intranasal infection and CIPS treatment: the antiviral effect of CIPS on SARS-CoV-2 infection in hACE2 mice was measured 3 days post-infection, with CIPS administered with the virus (**a**) and before (prophylactic) or after (therapeutic) virus infection (**b**). The presence of SARS-CoV-2 in the lung was assessed and is expressed as the number of SARS-CoV-2 RNA copies per microgram of total RNA (mean \pm s.e.m. of $n=3$ mice). **c**, Representative H&E-stained images of lung 3 days after infection with SARS-CoV-2 without and with treatment with CIPS. Green arrow, alveolar septal thickening; blue arrow, bronchial epithelial denudation, loss of cilia; black arrows, inflammatory cell infiltration. **d**, CIPS treatment reduced gene expression of inflammatory factors in mouse lung. Gene expression was assessed by quantitative PCR (qPCR). *Actin* was used as the housekeeping gene, and relative gene expression is normalized to the Ctrl. Genes encoding interleukin (IL)-1 β (*IL1B*), IL-6 (*IL6*), interferon (IFN)- β (*IFN β*) and IFN- γ (*IFN γ*) were evaluated. Mean \pm s.e.m. of $n=3$ mice. Statistical significance was calculated by one-way ANOVA with Tukey's multiple comparisons test.

trap the authentic SARS-CoV-2 virus (Fig. 3a,b) as well as the isolated S protein (Supplementary Fig. 8e). We determined that CIPS binds to the S-protein RBD with a very high binding affinity (dissociation constant (K_D) < 0.001 nM, Fig. 3c), compared with at least a 100-fold lower affinity for other serum proteins and factors (Fig. 3d and Supplementary Table 3), suggesting a selective binding capacity for the RBD. In complex media (reproduced with excess volumes of mouse lung homogenates or fetal bovine serum), CIPS retained a strong binding capacity for the S protein of SC2-P (Supplementary Fig. 8f,g) and full antiviral capacity (Fig. 3e and Supplementary Fig. 8h). Other 2D NMs (MoS₂ and graphene oxide (GO)) showed a significantly lower capacity to bind the RBD (K_D = 11.7 and 5.2 nM, respectively; Supplementary Fig. 9), with their K_D (CIPS \ll GO < MoS₂) correlating to their antiviral activity (Extended Data Fig. 1b). The binding of the RBD to ACE2 (K_D = 11–17.4 nM, in agreement with reported data³⁶) was totally abolished if the RBD was pre-exposed to CIPS, even at the lowest tested concentration (15 fM; Fig. 3f). Compared with a commercial mAb, CIPS showed a substantially higher inhibitory capacity (Fig. 3f and Supplementary Fig. 10), with a calculated inhibition constant (K_i) of 0.053 fM for CIPS compared with 75 pM for the mAb.

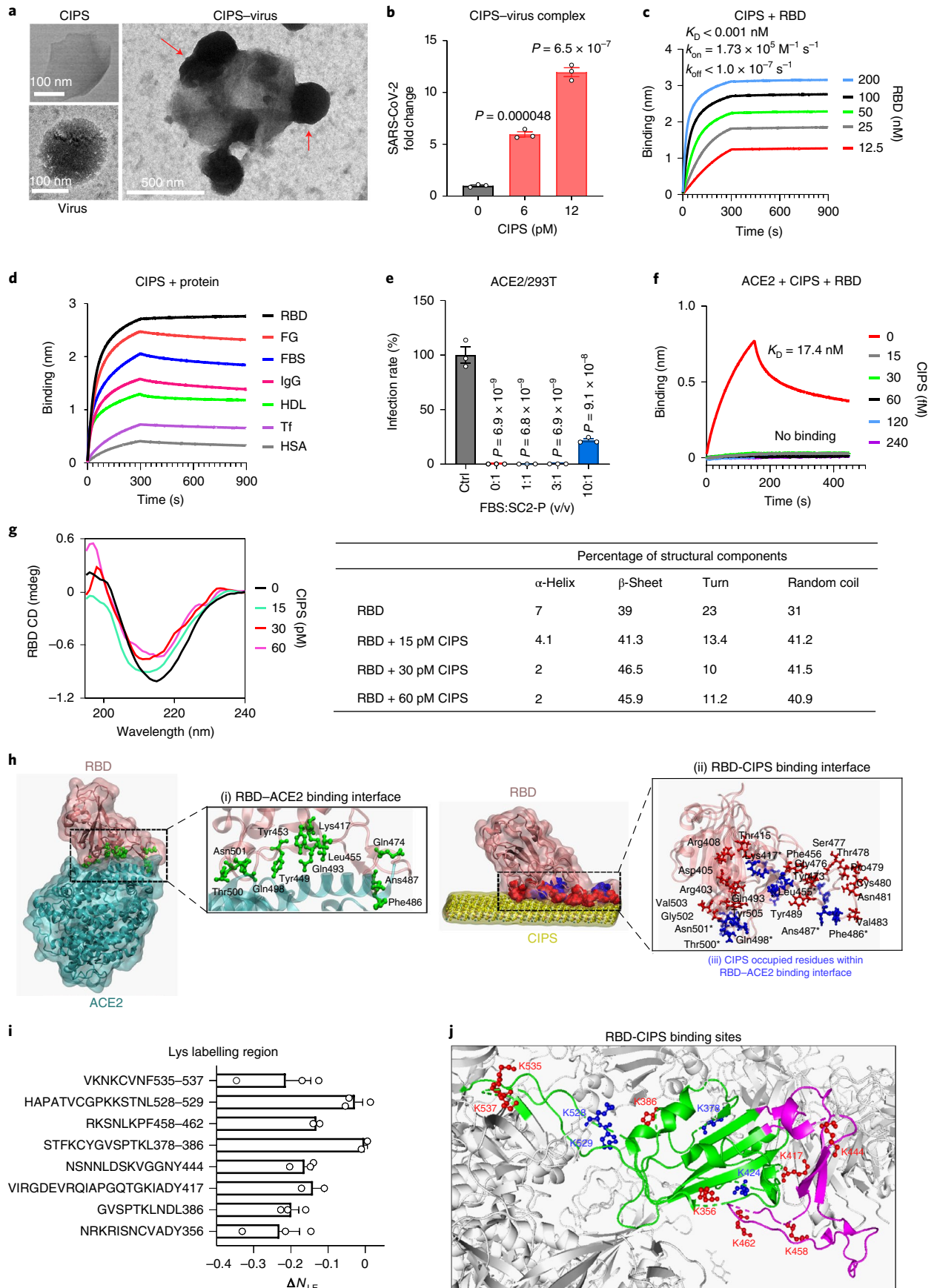
A molecular dynamics (MD) simulation was performed to study the adsorption of the RBD on the CIPS surface, using the crystal structures of ACE2 and the S protein to elucidate their binding interface (Supplementary Fig. 11). The amino acid residues of the RBD that bind to ACE2 are listed in Extended Data Fig. 3. The secondary structure of the RBD in the absence or presence of CIPS was characterized by circular dichroism (CD) spectroscopy, which showed that the majority of the RBD structure exists as the β -sheet conformation (Fig. 3g). As β -sheet structures promote protein adsorption on NSs³⁹, this may explain the preferential binding of the RBD to CIPS. A conformational change in the RBD upon CIPS binding was also observed (Fig. 3g), with a decrease in the amount of α -helix and turn conformations, and an increase in the β -sheets and random coils. A MD simulation was further performed to explore the binding interface of the RBD with CIPS within 100 ns (Supplementary Figs. 12 and 13 and Supplementary Table 4). Extended Data Fig. 4 shows the typical configurations with increasing time, with the amino acid residues and the interactive forces contributing to the binding illustrated in different colours. Among the eleven amino acid residues of the RBD interacting with the ACE2, eight residues bind to the surface of CIPS (Extended Data Fig. 3, indicated by *).

Hydrophobic, polar and positively charged residues in the RBD mainly contribute to its adsorption on CIPS (Supplementary Table 5). The functional groups (-NH₃⁺, -OH, -CONH₂, -C₆H₅, -H, -CH₃ and -SH) in the amino acid residues are involved in the adsorption on CIPS, whereby, based on the calculated interaction energies, the positively charged residues (Arg, Lys: -NH₃⁺) and the polar residues

(Ser, Tyr, Thr: -OH) can be considered the most important interacting residues (Supplementary Table 4). The adsorption reaches equilibrium after ~41.4 ns of the 100 ns simulation (Extended Data Fig. 4). Among the amino acid residues critically involved in the RBD-ACE2 binding (shown in green in Fig. 3h(i)), eight out of eleven are located in turn regions of the RBD (Fig. 3h(ii), Extended Data Fig. 3 and Supplementary Table 5) at 100 ns simulation, depicted in blue and common both the RBD-ACE2 and RBD-CIPS systems (Fig. 3h(iii)). As the interaction with CIPS leads to a decrease in the proportion of turn conformation in the RBD (Fig. 3g), the turn conformation will probably be disrupted, thereby changing the binding interface of the RBD with ACE2 and inhibiting the virus interaction with host cells. We also identified the potential binding sites and regions of the RBD for CIPS by mass spectrometry (MS)-based two-step isotope labelling lysine reactivity profiling (TILLRP)⁴⁰. We observed that lysine labelling levels in the RBD-CIPS complex were significantly reduced at six lysine sites or in their neighbouring regions in the RBD (Lys356, Lys386, Lys417, Lys444, Lys458-Lys462 and Lys535-Lys537; Fig. 3i), suggesting that their surroundings can be blocked by CIPS. According to the conformational structure of the RBD, different peptide fragments, including Val401-Tyr421 (Lys417), Asn437-Tyr449 (Lys444), Arg457-Phe464-Tyr508 (Lys458, Lys462), are probably involved in the binding with CIPS. Indeed, MD simulations indicate that almost all binding residues are located in the three above-mentioned regions (shown in green and purple in Fig. 3j). In detail, six residues, namely Arg403, Asp405, Arg408, Thr415, GLY416 and Lys417, are found in the region Val401-Tyr421, and two residues, that is, Leu455 and Phe456, are located close to the Asn437-Tyr449 domain. Another 19 residues are located in the region Arg457-Phe464-Tyr508. The conformational structure of the ACE2-RBD complex indicates that eight of the eleven amino acids of the RBD binding site (Extended Data Fig. 3) are located in the Arg457-Phe464-Tyr508 and Val401-Tyr421 regions. Thus, the MS and MD simulation results coincide in the identification of the CIPS-RBD binding sites, and show that binding to CIPS engages the same RBD residues involved in ACE2 binding, thereby confirming the anti-SARS-CoV-2 capacity of CIPS.

We performed further MD simulations to compare the binding of the RBD to CIPS and other materials. Compared with the binding of the RBD to GO and MoS₂ NSs (Supplementary Figs. 14 and 15 and Supplementary Table 6), CIPS exhibits the lowest interaction energy (corresponding to the strongest binding interaction; Supplementary Fig. 15b), the highest contact atom number (Supplementary Fig. 15c) and the greatest contact area (Supplementary Fig. 15d). Thus, the higher binding affinity of CIPS for the RBD can also be attributed to its stronger electrostatic attraction, with the simulation data (Supplementary Fig. 15) being consistent with the binding (Supplementary Fig. 9) and infection data (Extended Data Fig. 1).

Fig. 3 | SARS-CoV-2 inhibition mechanism of CIPS. **a**, TEM images depicting the interaction between SARS-CoV-2 and CIPS. The red arrows indicate virus particles adhering to CIPS. **b**, CIPS binding to SARS-CoV-2 after incubation of CIPS with the virus, followed by centrifugation. SARS-CoV-2 was assessed in CIPS precipitates. Mean \pm s.e.m. of $n=3$ biological replicates, from one representative experiment out of $n=2$ performed. **c,d**, Binding affinity of CIPS to RBD (**c**) and other proteins (**d**), determined by bilayer interferometry (BLI). FG, fibrinogen; FBS, fetal bovine serum; IgG, immunoglobulin G; HDL, high density lipoprotein; Tf, transferrin; HSA, human serum albumin. **e**, Inhibition of SC2-P by CIPS in complex biological matrices. SC2-P admixed with CIPS and FBS was used to infect ACE2/293T cells. Mean \pm s.e.m. of $n=3$ biological replicates from one experiment representative of $n=3$ performed. **f**, Inhibition of ACE2-RBD binding by CIPS determined by BLI. **g**, Conformational variation of the RBD after CIPS interaction, determined by CD spectra. **h**, MD simulation of the ACE2-RBD and CIPS-RBD binding interfaces. Amino acid residues at the RBD binding sites with ACE2 (i, green) and with CIPS (System 1, see Supplementary Fig. 13; ii, red and blue) largely overlap (iii, blue, highlighted with an asterisk). **i**, Variations in the relative native Lys labelling efficiency (N_{LE}) for the CIPS-bound RBD compared with the RBD. Lys residues were labelled with isotope dimethyl tags, and N_{LE} was detected and quantified by MS-based TILLRP. Mean \pm s.e.m. of $n=3$ independent experiments. **j**, Schematic diagram of the binding interface between CIPS and the RBD of the spike protein S1. The S1 conformation is shown in grey, and its RBD is shown in other colours. The RBD encompasses two regions in the RBD-CIPS interaction, the region N437-Y508 (purple), showing the strongest binding efficiency, and the remaining part (green). The RBD Lys sites of the RBD with decreasing N_{LE} after interacting with CIPS (red) and the surrounding regions are considered potential binding sites. Lys residues in blue are not located in the RBD-CIPS binding regions and/or fail to be detected by MS, with little alteration in reactivity during the formation of the RBD-CIPS complexes. In **b** and **e**, statistical significance was calculated by one-way ANOVA with Tukey's multiple comparisons test.



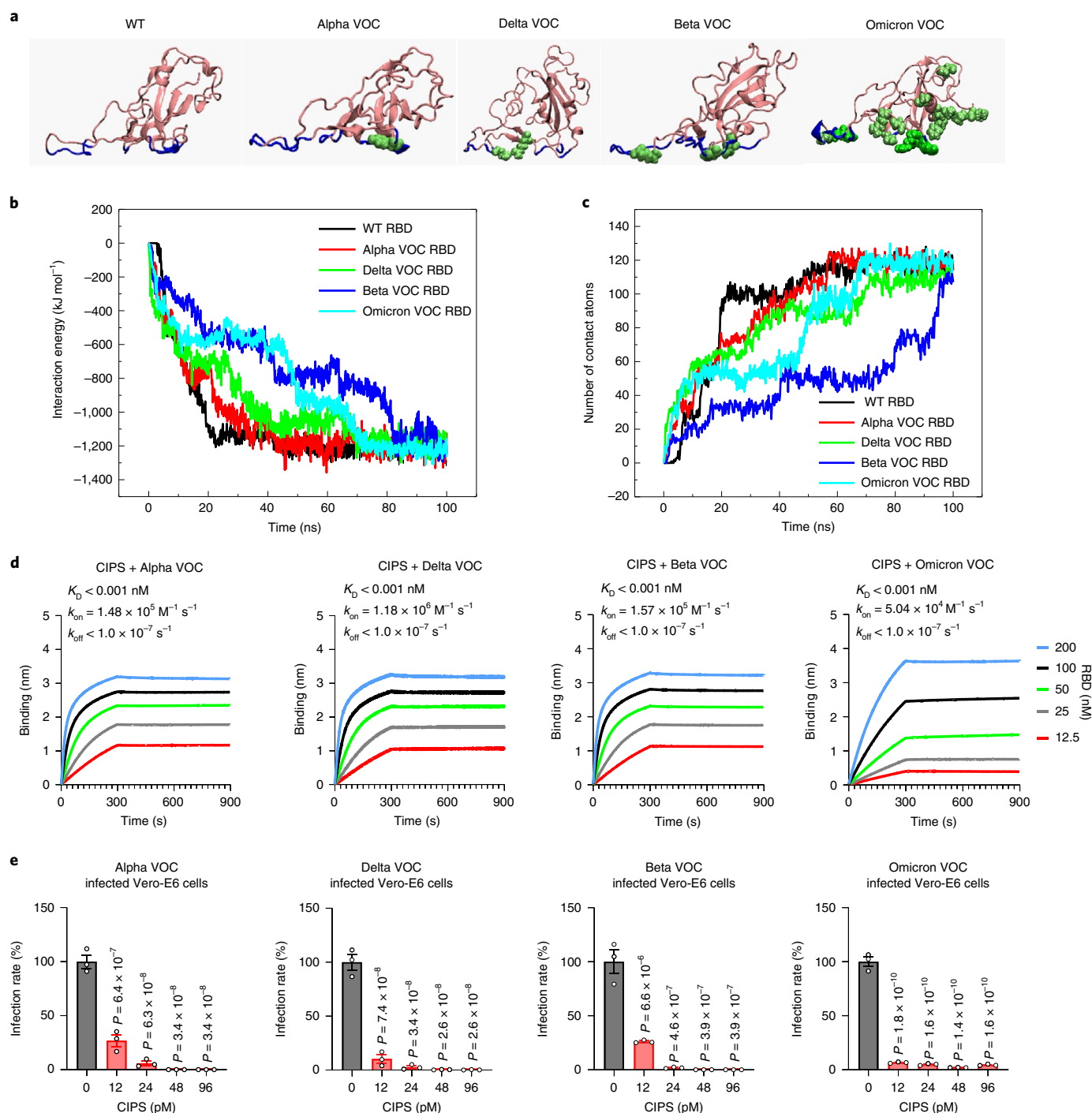


Fig. 4 | Antiviral effect of CIPS against SARS-CoV-2 VOCs. **a**, Representative configurations and adsorption interfaces of the wild-type (WT) and mutant RBDs. The mutated residues in the VOC RBDs are shown in green. The residues at the binding interface with CIPS are shown in blue. **b,c**, Interaction energy between the RBDs and CIPS (**b**) and the number of contact atoms (**c**) in the RBD when approaching the CIPS surface. **d**, Binding affinity between CIPS and the mutant RBDs of SARS-CoV-2 VOCs, measured by BLI. CIPS was immobilized on the BLI sensor and immersed in mutant RBD solutions. **e**, CIPS inhibits the in vitro infectivity of SARS-CoV-2 VOCs. The antiviral effect of CIPS was measured on Vero-E6 cells 48 h after infection by SARS-CoV-2 VOCs in the absence or presence of CIPS. SARS-CoV-2 ORF1ab was quantitatively evaluated by real-time PCR (rtPCR). Mean \pm s.e.m. of $n=3$ biological replicates. Statistical significance was calculated by one-way ANOVA with Tukey's multiple comparisons test.

CIPS effectively inhibits infection by SARS-CoV-2 VOCs

The majority of therapeutic mAbs developed against the SARS-CoV-2 RBD are ineffective against the Omicron VOC^{15,16,41}, thereby increasing the need for new antivirals with a broad activity spectrum. MD simulations of the interaction between CIPS and the

VOCs RBDs (Fig. 4a,b) show that the interaction energy and the number of contact atoms of CIPS with the VOCs RBDs are similar to those observed with the wild-type SARS-CoV-2 RBD (Fig. 4b,c, Extended Data Fig. 5 and Supplementary Table 5), suggesting that CIPS interacts similarly with all SARS-CoV-2 RBDs. Analysis of

the binding with the Omicron RBD showed that CIPS can bind to 10 of the 17 RBD residues involved in binding to ACE2 (Extended Data Fig. 6). Importantly, CIPS displays a very high binding affinity for all SARS-CoV-2 VOCs, with similar K_D values of less than 1 pM (Fig. 4d). The antiviral effect of CIPS against the SARS-CoV-2 VOCs was significant for all VOCs (Fig. 4e), and comparable to that observed for wild-type SARS-CoV-2.

CIPS promotes SARS-CoV-2 elimination by macrophages

We investigated whether macrophages could better phagocytose and eliminate the virus when bound to CIPS. Indeed, CIPS-associated SC2-P could be effectively phagocytosed by human macrophages after 24 h incubation, and the virus was effectively eliminated during the subsequent degradation process (Fig. 5a,b). SC2-P accumulated in macrophages after lysosomal inhibition with bafilomycin (BM; Fig. 5a,b) and colocalized with lysosomes (Fig. 5c), suggesting that the majority of SC2-P was degraded in phagolysosomes. Likewise, experiments with authentic SARS-CoV-2 virus showed that CIPS-associated SARS-CoV-2 could be effectively taken up and eliminated by macrophages (Fig. 5d,e), and that lysosome inhibition with BM significantly increased intracellular levels of SARS-CoV-2, implying that SARS-CoV-2 elimination was lysosome-dependent (Fig. 5e).

We examined whether virus uptake by macrophages exclusively led to virus degradation or whether it could also lead to cell infection. With both SC2-P and authentic SARS-CoV-2 virus, we observed that uptake of CIPS-associated virus did not cause macrophage infection, as virus release in culture could not be observed (Fig. 5f,g). This suggests that macrophages can efficiently take up and eliminate SARS-CoV-2 when associated with CIPS. The role of macrophages in CIPS-promoted virus elimination was further suggested by *in vivo* data from hACE2 transgenic mice, which showed that CIPS treatment, in parallel with suppressing SARS-CoV-2 replication, enhanced the colocalization of SARS-CoV-2 and macrophages in the lung (Fig. 5h).

Transmission X-ray microscopy imaging combined with nano-computer tomography (Nano-CT) was used to visualize intracellular CIPS, and showed a substantial accumulation of CIPS in cells after 12 h exposure and a strong decrease in intracellular CIPS after 48 h in CIPS-free medium (Fig. 5i). Based on the results of an inductively coupled plasma mass spectrometry (ICP-MS) analysis for indium content, macrophages took up CIPS in a time-dependent fashion, and following CIPS removal from the medium the content of indium decreased with time (Fig. 5j). Both the imaging and

quantitative results suggest CIPS degradation by macrophages. Cu XANES was used to quantify the chemical changes in CIPS during accumulation and degradation in macrophages. The results show that the speciation of Cu in internalized CIPS was +1, and that Cu was present in the chemical form of Cu-S. With increasing time, the speciation of Cu in macrophages changed from +1 to +2, and the chemical form of Cu changed from Cu-S to Cu-O/Cu-OOC (Fig. 5k,l and Supplementary Table 2), suggesting that during intracellular trafficking CIPS changed from oxidation to degradation, most probably in acidic phagolysosomes. The biodistribution and elimination of CIPS *in vivo* were also monitored, showing a maximal accumulation of CIPS in the lung at 6 h and almost entire elimination after 7 days (Fig. 5m,n, Supplementary Table 7 and Extended Data Fig. 7a), with a clear association of CIPS with macrophages (Fig. 5o).

A detailed chemical analysis of CIPS-dependent viral elimination in macrophages showed that copper ions (Cu^+ and Cu^{2+}) promoted the generation of hydroxyl radicals from H_2O_2 in lysosome-like acidic conditions (Supplementary Fig. 16). The strong oxidative capacity of hydroxyl radicals is expected to damage the viral structure and components such as proteins, lipids and nucleic acids (see Supplementary Fig. 17a,c,e for examples with prototypical molecules), as demonstrated with the entire pseudovirus (Supplementary Fig. 17b,d,f).

To investigate whether phagocytosis of CIPS-associated SARS-CoV-2 could promote protective immunity, we examined the capacity of CIPS to upregulate the expression of molecules involved in macrophage activation and antigen presentation. Compared with cells exposed to the virus alone, CIPS upregulated the expression of CD86 and HLA-DRA, two important molecules for antigen presentation, in SARS-CoV-2 co-treated macrophages (Fig. 5p). These results suggest that CIPS-bound SARS-CoV-2 could promote antigen presentation in the context of MHC II molecules in macrophages, thereby potentially triggering an adaptive antiviral immune response.

Conclusions

Here we have described the 2D CIPS NS as an effective nano-glue capable of selectively capturing the SARS-CoV-2 virus by binding its S protein, thereby inhibiting infection of host cells. The binding affinity of CIPS to the S-protein RBD is <1 pM, suggesting the formation of very stable complexes. The effective binding of CIPS to eight of the eleven ACE2-binding amino acid residues of the SARS-CoV-2 RBD accounts for the efficient inhibition of viral

Fig. 5 | CIPS promotes the phagocytosis and elimination of SARS-CoV-2 by macrophages. **a**, Immunofluorescence (IF) images of phagocytosis and elimination of SC2-P (red) in the absence or presence of CIPS in THP-1 differentiated macrophages. Mock, solvent of BM. Scale bars, 10 μm . **b**, Quantitative analysis of SC2-P phagocytosis and elimination. **c**, Colocalization (yellow) of SC2-P (red) and lysosomes (green) in macrophages observed in the phagocytosis/uptake period. **d**, Intracellular SARS-CoV-2 was evaluated in macrophages exposed to SARS-CoV-2 for phagocytosis and subsequent degradation. **e**, Intracellular SARS-CoV-2 was assessed in macrophages exposed to virus pre-incubated with CIPS in the absence or presence of BM. **f,g**, Macrophages were not infected by SC2-P (**f**) or SARS-CoV-2 (**g**) *in vitro*. SC2-P infection was assessed by luciferase activity (RLU, relative luciferase unit) (**f**), and SARS-CoV-2 infection was evaluated as virus copies in cell culture medium by qPCR (**g**). ND, not detected. **h**, Colocalization of macrophages and SARS-CoV-2 on treatment with CIPS *in vivo*. Representative immunofluorescence images of mouse lung are shown 3 days after SARS-CoV-2 infection. Scale bars, 10 μm . **i**, Three-dimensional tomographic images showing the intracellular accumulation of CIPS after the uptake and degradation periods, observed by soft transmission X-ray microscopy (Nano-CT). **j**, Uptake and degradation of CIPS by macrophages measured at different times, determined by ICP-MS. **k,l**, Chemical transformation and degradation of intracellular CIPS during uptake and degradation: the chemical species of Cu in reference samples (**k**) and in intracellular CIPS (**l**) were determined by Cu K-edge XANES. The percentages of the different chemical forms of Cu before and after interaction with macrophages are reported in Supplementary Table 2. **m,n**, Chemical transformation and clearance of CIPS in mouse lung after a single intranasal instillation of CIPS: Cu chemical forms were determined by XANES (**m**), and elemental mapping of Cu was observed by X-ray fluorescence (XRF) (colour bar shows fluorescence intensity ranging from 0 to 100) (**n**). Scale bars, 2 mm. **o**, Colocalization of CIPS with macrophages in mouse lung. Macrophages were stained with anti-F4/80 and imaged by immunofluorescence. Cu mapping was observed by XRF. **p**, CD86 and HLA-DRA (human leukocyte antigens DR alpha) gene expression in macrophages exposed to SARS-CoV-2 in the absence or presence of CIPS for 48 h. The gene encoding glyceraldehyde-3-phosphate dehydrogenase (*GAPDH*) was used as the housekeeping gene, and the relative gene expression was normalized to the virus infection group. For **b,d-g,j** and **p**, mean \pm s.e.m. of $n=3$ biological replicates. Statistical significance was calculated by two-way ANOVA with Tukey's multiple comparisons test in **b** and **e**, and by the two-tailed Student's *t*-test in **d,f,g** and **p**.

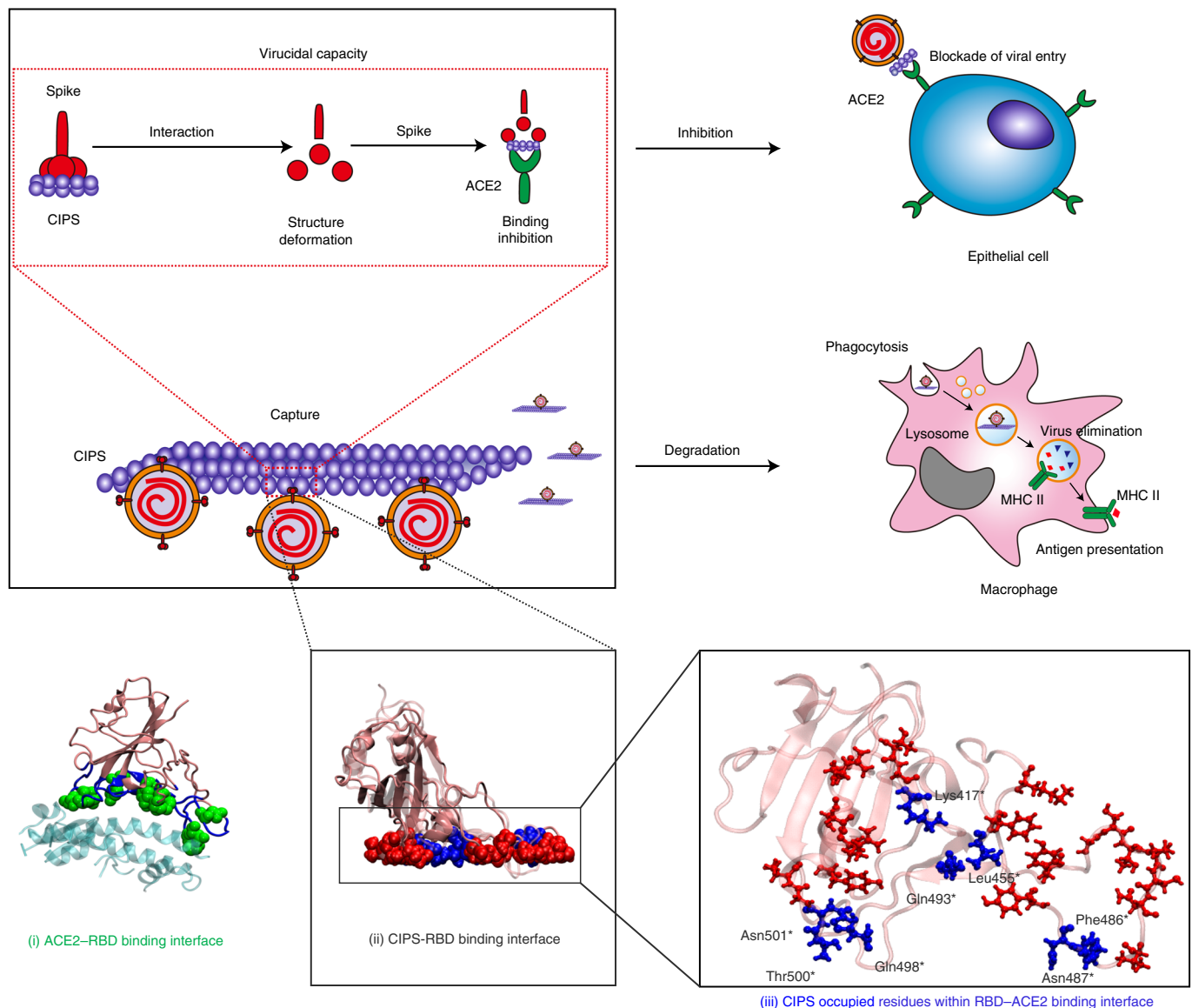


Fig. 6 | The anti-SARS-CoV-2 capacity of the CIPS 'nano-glue'. The proposed mechanisms by which CIPS can promote SARS-CoV-2 elimination are depicted. CIPS can strongly interact with the viral S-protein RBD and cause its deformation. Amino acid residues at the ACE2-RBD binding site (i) and those for CIPS-RBD binding (ii) largely overlap (iii, blue residues, highlighted with an asterisk). Strong binding to CIPS prevents interaction of the viral RBD with ACE2 on host cells and the consequent virus infectivity. Further, CIPS-trapped SARS-CoV-2 can be efficiently phagocytosed by macrophages, leading to virus degradation in phagolysosomes with the possible generation of viral peptides, which, together with the concomitant upregulation of antigen-presenting molecules on macrophages, is the basis for the initiation of virus-specific adaptive immunity.

infectivity. The RBD mutations displayed by SARS-CoV-2 VOCs do not affect their binding to CIPS, and indeed CIPS proved broadly effective in inhibiting all the viral VOCs, with efficacy evident in both preventive treatment and therapeutic strategies in vitro and in vivo. In addition, the similarity of the RBD of SARS-CoV-2 to the RBDs of other coronaviruses (for example, SARS) suggests that CIPS is also potentially useful in broadly inhibiting coronavirus infectivity (Supplementary Fig. 18).

Notably, the affinity of CIPS for SARS-CoV-2 RBDs ($K_D < 1$ pM) is substantially higher than that of therapeutic mAbs, which have an affinity in the range from 23 pM to 100 nM^{25,28,42}, similar to the binding affinity between the RBD and ACE2 (11–17.4 nM in our hands, 14.7 nM reported for S-protein binding to ACE2³⁶). This suggests that only a few of the currently available mAbs may have sufficient affinity for the RBD to efficiently compete with its binding to ACE2,

and that their efficacy against different VOCs varies greatly, with a substantial loss of efficacy for the Omicron VOC, which displays 15 mutations in the RBD¹⁵. Thus, compared with mAbs, CIPS displays a higher affinity for RBD and a broader specificity, which enable it to bind and neutralize all SARS-CoV-2 VOCs.

CIPS has been found safe and biocompatible both in vitro (Supplementary Fig. 4) and in vivo (Extended Data Fig. 7, Supplementary Figs. 19 and 20, and Supplementary Tables 8 and 9), being quickly removed from the lung, most probably degraded by macrophages, and eliminated through urine (Extended Data Fig. 7d). After intranasal administration, CIPS does not enter the blood stream (Extended Data Fig. 7), is unable to cause haemolysis, does not induce inflammatory activation of macrophages and is unable to bind IgG (Supplementary Fig. 21). The SARS-CoV-2 adsorbed on CIPS can be efficiently phagocytosed by macrophages,

shuttled to phagolysosomes and completely degraded together with its carrier. Another important consequence of the CIPS-dependent virus uptake by macrophages and its intracellular degradation is the expected generation of viral peptides and their presentation in the context of MHC II molecules, that is, the pathway of antigen presentation that induces a strong antibody response. Thus, the capacity of CIPS to direct the virus to macrophages has the double advantage of promoting viral destruction and triggering antiviral adaptive immunity.

Thus, CIPS is a safe, biocompatible and biodegradable 2D NM capable of inhibiting infection and promoting the elimination of SARS-CoV-2 (Fig. 6). The binding between CIPS and the SARS-CoV-2 S-protein RBD is ~10,000-fold stronger than the affinity of the virus for ACE2, suggesting that the CIPS-captured virus will not be released and will not infect cells. Notably, CIPS binding is 23- to 100-fold stronger than that of the best mAbs, and its broad capacity for RBD binding makes it equally effective against all the tested VOCs, as well as for other coronaviruses. Its broad-spectrum efficacy, storage stability and good biocompatibility make CIPS a promising anti-SARS-CoV-2 drug candidate. The viscous flypaper-like and selective binding capacity of CIPS for the SARS-CoV-2 S protein also makes it particularly promising as a surface-coating material and decontamination agent, to contain viral spread and increase safety during handling in laboratory and clinical settings.

Online content

Any methods, additional references, Nature Research reporting summaries, source data, extended data, supplementary information, acknowledgements, peer review information; details of author contributions and competing interests; and statements of data and code availability are available at <https://doi.org/10.1038/s41565-022-01177-2>.

Received: 9 February 2021; Accepted: 13 June 2022;
Published online: 22 August 2022

References

- Wu, D., Wu, T., Liu, Q. & Yang, Z. The SARS-CoV-2 outbreak: what we know. *Int. J. Infect. Dis.* **94**, 44–48 (2020).
- Wang, M. et al. Remdesivir and chloroquine effectively inhibit the recently emerged novel coronavirus (2019-nCoV) in vitro. *Cell Res.* **30**, 269–271 (2020).
- Chen, Y. et al. Research progress of chloroquine and hydroxychloroquine on the COVID-19 and their potential risks in clinic use. *Front. Pharmacol.* **11**, 1167 (2020).
- Beigel, J. H. et al. Remdesivir for the treatment of Covid-19—final report. *N. Engl. J. Med.* **383**, 1813–1826 (2020).
- Mahase, E. Covid-19: Pfizer's paxlovid is 89% effective in patients at risk of serious illness, company reports. *Brit. Med. J.* **375**, n2713 (2021).
- Mahase, E. Covid-19: UK becomes first country to authorise antiviral molnupiravir. *Br. Med. J.* **375**, n2697 (2021).
- Bull-Otterson, L. et al. Hydroxychloroquine and chloroquine prescribing patterns by provider specialty following initial reports of potential benefit for COVID-19 treatment—United States, January–June 2020. *MMWR Morb. Mortal. Wkly Rep.* **69**, 1210–1215 (2020).
- FDA cautions against use of hydroxychloroquine or chloroquine for COVID-19 outside of the hospital setting or a clinical trial due to risk of heart rhythm problems. *Food and Drug Administration* <https://www.fda.gov/drugs/drug-safety-and-availability/fda-cautions-against-use-hydroxychloroquine-or-chloroquine-covid-19-outside-hospital-setting-or> (2020).
- Geleris, J. et al. Observational study of hydroxychloroquine in hospitalized patients with Covid-19. *N. Engl. J. Med.* **382**, 2411–2418 (2020).
- Skipper, C. P. et al. Hydroxychloroquine in nonhospitalized adults with early COVID-19: a randomized trial. *Ann. Intern. Med.* **173**, 623–631 (2020).
- Wang, Y. et al. Remdesivir in adults with severe COVID-19: a randomised, double-blind, placebo-controlled, multicentre trial. *Lancet* **395**, 1569–1578 (2020).
- Cohen, J. & Kupferschmidt, K. 'A very, very bad look' for remdesivir. *Science* **370**, 642–643 (2020).
- Pan, H. et al. Repurposed antiviral drugs for COVID-19—interim WHO Solidarity trial results. *N. Engl. J. Med.* **384**, 497–511 (2020).
- Fiorentini, S. et al. First detection of SARS-CoV-2 spike protein N501 mutation in Italy in August, 2020. *Lancet Infect. Dis.* **21**, e147 (2021).
- Takashita, E. et al. Efficacy of antibodies and antiviral drugs against Covid-19 Omicron variant. *N. Engl. J. Med.* **386**, 995–998 (2022).
- Cao, Y. et al. Omicron escapes the majority of existing SARS-CoV-2 neutralizing antibodies. *Nature* **602**, 657–663 (2022).
- Ali, M. J. et al. Treatment options for COVID-19: a review. *Front. Med.* **7**, 480 (2020).
- Chakraborty, D. et al. Exploring repurposing potential of existing drugs in the management of COVID-19 epidemic: a critical review. *J. Clin. Med. Res.* **12**, 463–471 (2020).
- Crosby, J. C. et al. COVID-19: a review of therapeutics under investigation. *J. Am. Coll. Emerg. Physicians Open* **1**, 231–237 (2020).
- Tai, W. et al. Characterization of the receptor-binding domain (RBD) of 2019 novel coronavirus: implication for development of RBD protein as a viral attachment inhibitor and vaccine. *Cell. Mol. Immunol.* **17**, 613–620 (2020).
- Brouwer, P. J. M. et al. Potent neutralizing antibodies from COVID-19 patients define multiple targets of vulnerability. *Science* **369**, 643–650 (2020).
- Pinto, D. et al. Cross-neutralization of SARS-CoV-2 by a human monoclonal SARS-CoV antibody. *Nature* **583**, 290–295 (2020).
- Ju, B. et al. Human neutralizing antibodies elicited by SARS-CoV-2 infection. *Nature* **584**, 115–119 (2020).
- Hansen, J. et al. Studies in humanized mice and convalescent humans yield a SARS-CoV-2 antibody cocktail. *Science* **369**, 1010–1014 (2020).
- Wu, Y. et al. A noncompeting pair of human neutralizing antibodies block COVID-19 virus binding to its receptor ACE2. *Science* **368**, 1274–1278 (2020).
- Li, W. et al. High potency of a bivalent human V_H domain in SARS-CoV-2 animal models. *Cell* **183**, 429–441 (2020).
- Yuan, M. et al. A highly conserved cryptic epitope in the receptor binding domains of SARS-CoV-2 and SARS-CoV. *Science* **368**, 630–633 (2020).
- Andreano, E. et al. Extremely potent human monoclonal antibodies from COVID-19 convalescent patients. *Cell* **184**, 1821–1835 (2021).
- Hoffmann, M. et al. SARS-CoV-2 variants B.1.351 and P.1 escape from neutralizing antibodies. *Cell* **184**, 2384–2393 (2021).
- Cheeseman, S. et al. Antimicrobial metal nanomaterials: from passive to stimuli-activated applications. *Adv. Sci.* **7**, 1902913 (2020).
- Cagno, V. et al. Broad-spectrum non-toxic antiviral nanoparticles with a virucidal inhibition mechanism. *Nat. Mater.* **17**, 195–203 (2018).
- Rupp, R., Rosenthal, S. L. & Stanberry, L. R. VivaGel (SPL7013 gel): a candidate dendrimer–microbicide for the prevention of HIV and HSV infection. *Int. J. Nanomed.* **2**, 561–566 (2007).
- Lara, H. H., Garza-Trevino, E. N., Ixtapan-Turrent, L. & Singh, D. K. Silver nanoparticles are broad-spectrum bactericidal and virucidal compounds. *J. Nanobiotechnol.* **9**, 30 (2011).
- Kim, J. et al. Porous gold nanoparticles for attenuating infectivity of influenza A virus. *J. Nanobiotechnol.* **18**, 54 (2020).
- Baker, N. A., Sept, D., Joseph, S., Holst, M. J. & McCammon, J. A. Electrostatics of nanosystems: application to microtubules and the ribosome. *Proc. Natl Acad. Sci. USA* **98**, 10037–10041 (2001).
- Wrapp, D. et al. Cryo-EM structure of the 2019-nCoV spike in the prefusion conformation. *Science* **367**, 1260–1263 (2020).
- Lan, J. et al. Structure of the SARS-CoV-2 spike receptor-binding domain bound to the ACE2 receptor. *Nature* **581**, 215–220 (2020).
- Walters, R. W. et al. Adenovirus fiber disrupts CAR-mediated intercellular adhesion allowing virus escape. *Cell* **110**, 789–799 (2002).
- Baimanov, D. et al. Immunological responses induced by blood protein coronas on two-dimensional MoS₂ nanosheets. *ACS Nano* **14**, 5529–5542 (2020).
- Liu, Z. Y. et al. Probing conformational hotspots for the recognition and intervention of protein complexes by lysine reactivity profiling. *Chem. Sci.* **12**, 1451–1457 (2021).
- Weisblum, Y. et al. Escape from neutralizing antibodies by SARS-CoV-2 spike protein variants. *eLife* **9**, e61312 (2020).
- Barnes, C. O. et al. SARS-CoV-2 neutralizing antibody structures inform therapeutic strategies. *Nature* **588**, 682–687 (2020).

Publisher's note Springer Nature remains neutral with regard to jurisdictional claims in published maps and institutional affiliations.

Springer Nature or its licensor holds exclusive rights to this article under a publishing agreement with the author(s) or other rightsholder(s); author self-archiving of the accepted manuscript version of this article is solely governed by the terms of such publishing agreement and applicable law.

© The Author(s), under exclusive licence to Springer Nature Limited 2022

Methods

Preparation of CIPS nanosheets. Bulk CIPS material was synthesized by solid-state reaction according to a previously published procedure⁴³. CIPS nanosheets were exfoliated from bulk CIPS crystals by Li intercalation using *n*-butyllithium assisted by ultrasonication. After exfoliation, the nanosheets were centrifuged at 1,500g for 20 min and then rinsed with ethanol twice to remove free *n*-butyllithium in the suspension. The collected suspension was finally lyophilized and stored in dry conditions at -20°C .

MS analysis of RBD–CIPS binding. *Sample preparation and MS analysis.* The RBD protein (40 μl , 0.5 mg ml^{-1} dissolved in PBS) was mixed with 40 μl CIPS (1 mg ml^{-1} dissolved in PBS) in a centrifuge tube, the final volume was brought to 200 μl with PBS and the mixture incubated at 37°C for 40 min. Afterwards, two-step isotope labelling of the native proteins was carried out. NaCNBD_3 (1.5 μl at 50 $\mu\text{g l}^{-1}$) and $^{13}\text{CD}_2\text{O}$ (1.5 μl at 2 wt%) were added to the samples for active protein labelling, incubated at 25°C for 5 min, mixed with 5 M NH_4OAc (1 μl) and freeze-dried. In the second step of the labelling process, each sample was redissolved in 90 μl denaturing solution (6 M guanidine hydrochloride (GUA)–50 mM HEPES, pH 7.4). Then, 10 μl of 0.4 M pyridine–borane and 1 μl of 4% CH_2O were added to each sample, which were then maintained at 37°C for 2 h to complete the dimethylation of the lysine residues. The labelling reaction was quenched by adding 1 μl of 5 M NH_4OAc . Next, the protein was extracted and hydrolysed with protease. After reaction, each sample was mixed with 200 μl of 10% ammonia, incubated at 37°C for 5 min and centrifuged at 23,000g at 4°C for 20 min to remove CIPS. The protein buffer system was exchanged into 6 M GUA–50 mM HEPES buffer solution by ultrafiltration with centrifugal ultrafiltration units with a nominal molecular weight cut-off of 3K. The proteins were then reduced with 5 mM tris (2-carboxyethyl) phosphine hydrochloride (TCEP) and sequentially alkylated with 10 mM iodoacetamide (IAA). The buffer system was again exchanged for 20 mM NH_4HCO_3 by centrifugal ultrafiltration. Finally, the proteins were enzymatically hydrolysed with chymotrypsin for 16 h at 37°C at a substrate/enzyme ratio of 1:25 (wt/wt). After enzymatic hydrolysis, the peptide samples were acidified with 10% trifluoroacetic acid (TFA), freeze-dried and stored at 80°C until analysis.

LC–MS analysis was performed using an Orbitrap Fusion Lumos Tribrid mass spectrometer coupled to a Vanquish Flex HPLC system (ThermoFisher Scientific). In brief, 1 μg peptide sample was first loaded onto a 5 $\text{cm} \times 150 \mu\text{m}$ C18 trap column with 3 μm C18 particles and separated on a 25 $\text{cm} \times 150 \mu\text{m}$ C18 capillary column with 2.4 μm C18 particles. The mobile phase of this reversed-phase HPLC system is composed of mobile phase A (0.1% formic acid (FA) in aqueous solution) and mobile phase B (0.1% FA in acetonitrile). The reversed-phase binary separation gradient was set as 0:100–5:95 (B:A, v:v) for 2 min, 5:95–35:65 (B:A, v:v) for 45 min, 35:65–80:20 (B:A, v:v) for 3 min and, after washing with 80:20 (B:A, v:v) for 5 min, the system was equilibrated with 100% mobile phase A for 15 min.

Data analysis. A database of RBD protein sequences was downloaded from UniProt (<http://www.uniprot.org>). Maxquant v.1.6.7, (<https://www.maxquant.org>) was used to search this database for the collected MS data. Quantification multiplicity was set to 5, and DimethylLys0, DimethylLys4A and DimethylLys8 were selected. Chymotrypsin was selected with a maximum missed cleavage of 5. The function of match between runs was enabled. The other parameters were set as default values. The native labelling efficiency (N_{LE}) values could be calculated from $N_{\text{LE}} = 1 - I_{\text{L}} / (I_{\text{H}} + I_{\text{M}} + I_{\text{L}})$, where I_{H} , I_{M} and I_{L} are the intensity of heavy, medium and light labelled peptide forms containing the corresponding lysine residues, respectively.

The RBD structure was adopted from the PDB file 7CZR. Based on the experimental results of lysine reactivity, protein display and structural analysis were performed by PyMOL v.1.9 (<https://pymol.org/2>).

CIPS effects on Vero-E6 cell infection by SARS-CoV-2 and its VOCs. The experiments were performed in a biosafety level 3 laboratory with standard regulations. SARS-CoV-2 (GDPCC-nCoV-8) and four VOCs (Alpha (GDPCC2.00304), Beta (GDPCC2.00004), Delta (GDPCC2.00096) and Omicron (GDPCC2.00297)) were isolated and typed in the laboratory of the Guangdong Center for Human Pathogen Culture Collection (GDPCC) and propagated on Vero-E6 cells.

For the infection experiments, Vero-E6 cells were seeded in 96-well plates at a density of 2×10^4 cells per well and cultured overnight. CIPS at various concentrations (1.5–96 μM) and SARS-CoV-2 or VOCs (50% tissue culture infectious dose (TCID₅₀) = 100) were added together to the Vero-E6 cells and incubated for 2 h. The cells were then washed twice with warm 1 × PBS and cultured for an additional 48 h with fresh cell culture medium (DMEM with 1% penicillin/streptomycin and 10% fetal bovine serum) or CIPS-containing medium. Non-infected cells and CIPS alone were used as controls. Supernatants were collected after 48 h, and SARS-CoV-2 was quantitatively analysed by rtPCR using a commercial COVID-19 detection kit (catalogue no. DA0931, DaAn Gene), targeting the nucleocapsid protein and open reading frame 1ab (ORF1ab). In brief, the nucleocapsid protein and ORF1ab were detected using FAM- and VIC-labelled TaqMan probes (Applied Biosystems 7500, ThermoFisher

Scientific). Amplification was performed as follows: 50°C for 15 min, 95°C for 15 min, followed by 45 cycles of 94°C for 15 s and 55°C for 45 s. For quantitative evaluation, plasmid standards were used to establish a standard curve by serial dilution (copy number versus fluorometric value), which was used to calculate the RNA copy number of SARS-CoV-2 from the fluorometric value of the samples. The standard curve is described by $y = 50 \times 10^{(12.352 - 0.2771 \times C_T)}$. The infection rate was calculated and normalized to virus infection controls. The condition of the Vero-E6 cells after SARS-CoV-2 infection was observed at 48 h, and optical microscopy images were acquired. The occupied space of the cells was analysed by ImageJ and the data are given as a percentage of the area covered by the cells, as an estimate of intact healthy cells in the image.

For the experiments assessing the post-infection effects of CIPS, Vero-E6 cells were seeded in 24-well plates at a density of 2×10^5 cells per well and cultured overnight. The cells were challenged with SARS-CoV-2 (50 TCID₅₀) for 2 h and then washed with PBS to remove non-internalized virus. The cells were then cultured in fresh medium or medium containing CIPS at various concentrations (24, 48 and 96 μM) for 48 h. The cells were collected and lysed with RNAluplus (Takara Bio). Intracellular SARS-CoV-2 was evaluated by qPCR for the S protein. Cellular 18S was used as housekeeping control.

The treatment window for CIPS was determined in vitro by adding CIPS to the culture medium at different times after SARS-CoV-2 challenge. Vero-E6 cells were seeded in 24-well plates at a density of 2×10^6 cells per well, cultured overnight and then challenged with SARS-CoV-2 (50 TCID₅₀). The virus-containing medium was discarded after 2 h and the infected cells were washed with PBS twice to remove free virus. Fresh medium was added and the culture continued until 48 h. Challenge with virus was considered as time 0. CIPS (12 μM) was added at time 0 or 2, 4 and 24 h after viral challenge. No CIPS treatment served as control. After 48 h, the culture medium was collected and the viral RNA was extracted using a High Pure Viral RNA Kit (Roche) and quantitated by rtPCR (QRZ-101, TOYOBO).

CIPS effects on SARS-CoV-2 infection of human airway epithelial tissue

cultures. A SARS-CoV-2 inoculum of 2×10^4 TCID₅₀ in 50 μl of the same medium as that used for the organoid culture was added to a single airway epithelial tissue-bearing transwell insert placed in the wells of a round-bottomed 24-well plate in the absence or presence of 24 μM CIPS and incubated at 37°C for 1 h. The inoculum was removed and the tissue-bearing inserts were washed three times with PBS to remove unbound virus. Each virus-infected tissue-bearing insert was transferred to a single well of a new 24-well plate (Corning) with 500 μl of fresh serum-free growth medium (cat. no. 05001, STEMCELL Technologies) or CIPS-containing medium, and incubated at 37°C with 5% CO_2 for 24 h. RNA extraction was performed after the addition of 150 μl Trizol (Qiagen) to the epithelial cell culture. The viral RNA in the collected samples was determined by qPCR with reverse transcription (RT–qPCR) using a SARS-CoV-2 diagnostic kit (cat. no. 2C-HX-201-2, BioGerm; approved by the China Center for Disease Control and Prevention) following the manufacturer's protocol. To examine the histological changes caused by SARS-CoV-2 infection and CIPS treatment, paraffin-embedded epithelia were sectioned at a thickness of 3 μm and examined after H&E staining. Immunofluorescence was performed with anti-acetyl- α -tubulin (Lys40) mouse mAb (cat. no. 6-11B-1) and anti-MUC5AC rabbit mAb (cat. no. E3O9I) from Cell Signaling Technology.

CIPS effects on SARS-CoV-2 infection of hACE2 transgenic mice in vivo.

Six- to eight-week-old male hACE2 transgenic mice were purchased from Gempharmatech (B6JGpt-Ace2^{tm1Cml/hACE2-stop}/Gpt, cat. no. T037630). The SARS-CoV-2 (National Microbiology Data Center accession number: NMDCN0000HUI, <https://nmdc.cn/resource/ncov/genome/detail/NMDCN0000HUI>) used for in vivo evaluation was kindly provided by the Guangdong Provincial Center for Disease Control and Prevention, Guangdong Province of China. SARS-CoV-2 challenge was performed in an animal biosafety level 3 facility at Kunming Institute of Zoology, Chinese Academy of Sciences (CAS). This animal experiment was performed in accord with the recommendations detailed in the Guide for the Care and Use of Laboratory Animals of Kunming Institute of Zoology, CAS, with approval ID IACUC-RE-2021-05-001 from the Institutional Animal Care and Use Committees of Kunming Institute of Zoology, CAS. Three mice per group were employed in the following experiments.

Mice were challenged with SARS-CoV-2 and CIPS by intranasal instillation (i.n.). The viral challenge (5×10^6 TCID₅₀ per mouse) was delivered in two 30 μl administrations 20 min apart to reduce animal discomfort and increase uptake. CIPS (4 and 8 mg per kg body weight, corresponding to 2.4 and 4.8 pmol per kg body weight) was administered with the first viral dose. After 3 days, the mice were sacrificed.

A second experiment was performed to compare therapeutic and prophylactic treatment with CIPS. Mice were challenged by i.n. with SARS-CoV-2 (1×10^6 TCID₅₀ per mouse, 30 μl), and CIPS (8 mg per kg body weight, corresponding to 4.8 pmol per kg body weight) was administered 1 h before (prophylactic) or after (therapeutic) viral infection. After 3 days, the mice were sacrificed.

RNA was extracted from lungs using RNAiso PLUS (Takara) according to the manufacturer's protocol. SARS-CoV-2 RNA in the lung was measured by RT-qPCR as previously reported⁴⁴. The results are expressed as the number of SARS-CoV-2 RNA copies per microgram lung total RNA. The standard curve for the calculation of RNA is described by $y = 0.87 \times 10^{2.3026} \times (-0.3297 \times C_T + 12.822)$. To assess the presence of pathological alterations, the lung tissue was examined by microscopic observation of histological sections stained with H&E. Immunofluorescence analysis was performed by staining with antibodies to F4/80 (GB11027, Servicebio Technology) for macrophages and against SARS-CoV-2 spike S1 (ABclonal) for SARS-CoV-2. The colocalization of SARS-CoV-2 with macrophages in the lung tissue following CIPS treatment was analysed by microscopy (VS200, Olympus).

SARS-CoV-2 association to CIPS. SARS-CoV-2 (1.2×10^4 TCID₅₀) was incubated with CIPS (6 and 12 pM in 200 µl PBS) for 1 h. Samples were centrifuged (1,000g for 5 min) to collect CIPS-trapped SARS-CoV-2 in precipitates. After RNA extraction, the presence of SARS-CoV-2 was quantitatively analysed by rtPCR for the S protein.

Determination of secondary structure of proteins by CD. The secondary structure of the RBD in the absence or presence of CIPS was assessed by CD (J-810, JASCO). The RBD (200 µg ml⁻¹ in 0.01 M phosphate buffer, pH 7.4) was mixed with CIPS (15, 30 and 60 pM) and then added to the cuvette with a thickness of 1 mm. CD spectra were collected between 190 and 250 nm. Each sample was measured six times and the spectra were averaged. The spectral data were processed using the CD Tool software (<http://cdtools.cryst.bbk.ac.uk>). The baseline (between 235 and 250 nm) was subtracted. Normalized data were analysed using DICROWEB to calculate the percentage of secondary structure, and the smoothed data are shown.

CIPS effects on the SC2-P interaction with macrophages. Cells of the human acute monocytic leukaemia cell line THP-1 were seeded in 24-well plates with a cover slide at 5×10^4 cells per well (for uptake/degradation), or in 96-well plates at 1×10^4 cells per well (for infection), and treated with 100 ng ml⁻¹ PMA for 24 h to induce macrophage differentiation.

For the uptake/degradation experiments, SC2-P (4×10^6 copies) was pre-incubated with CIPS (12 pM) for 2 h and then added to macrophages for 24 h (uptake period). The SC2-P-containing medium was then replaced with fresh medium, and the culture continued for another 24 h (degradation period). The lysosomal inhibitor BM (100 nM; MedChemExpress) was added to macrophages 6 h before the end of culture. The uptake and degradation of SC2-P were detected by immunofluorescence, and the colocalization of SC2-P and lysosomes was assessed by immunofluorescence. Lysosome and SC2-P were stained with antibodies to LAMP-1 (cat. no. NBP2-52721, Novus Biologicals) and anti-Flag (cat. no. AF0036, Beyotime Biotechnology), respectively.

For the infection experiments, macrophages were cultured with SC2-P (2×10^5 copies) for 24 h in the absence or presence of CIPS (24 pM), and then washed with PBS to remove extracellular virus. Cells were cultured with fresh medium for an additional 24 h. BM (100 nM) was added at 18 h. Cells were then lysed for luciferase evaluation (cat. no. E1910, Promega).

CIPS effects on the SARS-CoV-2 interaction with macrophages. The experiments were performed in a biosafety level 3 laboratory with standard regulations. The differentiation of THP-1 cells to macrophages was performed as described above in 24-well plates with 2×10^5 cells per well.

For the uptake/degradation experiments, SARS-CoV-2 (2.4×10^4 TCID₅₀) was added to macrophages for 4 h (uptake period). The cells were then washed twice with warm PBS and cultured for an additional 48 h with fresh medium (degradation period). RNA was extracted from the macrophages with RNAplus, and intracellular SARS-CoV-2 was evaluated quantitatively by rtPCR for the S protein.

The CIPS effect was evaluated by pre-incubating the authentic SARS-CoV-2 virus (2.4×10^4 TCID₅₀) with CIPS (12 pM) for 2 h, and then adding the virus (with or without CIPS pretreatment) to macrophages in culture for 48 h in the absence or presence of BM (100 nM). The macrophages were washed twice with PBS before RNA extraction and quantitative evaluation of SARS-CoV-2.

For the infection experiments, CIPS (12 pM) was pre-incubated with authentic SARS-CoV-2 virus (2.4×10^4 TCID₅₀) for 2 h. Macrophages were exposed to SARS-CoV-2 (pre-incubated or not with CIPS as described above) for 4 h, washed twice with PBS and cultured in fresh medium with or without BM (100 nM) for an additional 48 h. The supernatants were collected and the presence of SARS-CoV-2 was quantitatively analysed by rtPCR using a commercial COVID-19 detection kit (DaAn Gene), targeting the nucleocapsid protein and ORF1ab.

Protein structures used in MD simulations. The structures of the complexes formed between ACE2 and the RBD of SARS-CoV-2 (Protein Data Bank (PDB) ID: 6M17)⁴⁵, the Alpha VOC (PDB ID: 7EKF)⁴⁶, Delta VOC (PDB ID: 7WBQ)⁴⁷, Beta VOC (PDB ID: 7EKG)⁴⁶, Omicron VOC (PDB ID: 7WBP)⁴⁷ and the SARS-CoV-2 spike complexed with neutralizing monoclonal antibody P5A-

I88_2B (PDB ID: 7CZR)⁴⁸ were obtained from the Research Collaboratory for Structural Bioinformatics PDB (www.rcsb.org). The crystal structures of the RBD complexes with ACE2 feature in the following figures: 6M17 in Figs. 3h, 4a and 6, Supplementary Figs. 11 and 13, and Extended Data Figs. 4 and 5; 7EKF in Fig. 4a and Extended Data Fig. 5; 7WBQ in Fig. 4a and Extended Data Fig. 5; 7EKG and 7EKC in Fig. 4a and Extended Data Fig. 5; 7WBP in Fig. 4a and Extended Data Figs. 5 and 6.

Statistical analysis. The results are presented as mean values of replicate experiments or replicate samples in one representative experiment, as indicated in the figure legends. Statistical significance was calculated by the two-tailed Student's *t*-test for comparisons of two groups, and by one- or two-way ANOVA with Tukey's or Sidak's multiple comparisons test. Statistical analysis was performed using GraphPad Prism and $P < 0.05$ was considered statistically significant.

Reporting summary. Further information on research design is available in the Nature Research Reporting Summary linked to this article.

Data availability

The data that support the findings of this study are available within the paper and its Supplementary Information files, or from the corresponding authors upon request. Source data are provided with this paper.

Code availability

The original analysis code for the MD simulation is kept at the Institute of High Energy Physics of CAS, and is available from the corresponding authors upon request.

References

- Maisonneuve, V., Evain, M., Payen, C., Cajipe, V. B. & Molinie, P. Room-temperature crystal-structure of the layered phase CuInP₂S₆. *J. Alloys Compd.* **218**, 157–164 (1995).
- Liu, F.-L. et al. Rapid generation of ACE2 humanized inbred mouse model for COVID-19 with tetraploid complementation. *Natl. Sci. Rev.* **8**, nwa285 (2020).
- Yan, R. H. et al. Structural basis for the recognition of SARS-CoV-2 by full-length human ACE2. *Science* **367**, 1444–1448 (2020).
- Han, P. et al. Molecular insights into receptor binding of recent emerging SARS-CoV-2 variants. *Nat. Commun.* **12**, 6103 (2021).
- Han, P. et al. Receptor binding and complex structures of human ACE2 to spike RBD from Omicron and Delta SARS-CoV-2. *Cell* **185**, e610 (2022).
- Yan, R. et al. Structural basis for bivalent binding and inhibition of SARS-CoV-2 infection by human potent neutralizing antibodies. *Cell Res.* **31**, 517–525 (2021).

Acknowledgements

The authors are grateful to D. Li, J. Nahar, K. Chen, T. Liu, X. Li, X. Lin, Y. Wang, Y. Qiu and Y. Zeng (Laboratory of Immunology and Nanomedicine of SIAT-CAS) for their kind help with the biosafety experiment, to K. Liu (IHEP), R. Qiao (NCNST) and X. Li (IHEP) for their kind help with ICP-MS/XRF/XAFS experiments, and to Boyubio Company for assistance with the MD simulations. The authors also acknowledge the support from the Directional Institutionalized Scientific Research Platform of Beijing Synchrotron Radiation Facility of CAS, and the technological support from the biological MS facility of Dalian Coherent Light Source and Kunming National High-Level Biosafety Research Center for Non-human Primates, Center for Biosafety Mega-Science, Kunming Institute of Zoology, CAS. This work was financially supported by the National Key R&D Program of China (grant nos. 2021YFE0113000 (to Y.L., F.-L.L. and G.W.), 2021YFA1200900 (to L.W. and C.C.) and 2020YFA0710702 (to L.W.)), the National Natural Science Foundation of China (grant nos. 32171390 (to Y.L.), 31971322 (to L.W.), 22027810 and 11621505 (to C.C.), and 32088101 (to F.W.)), the CAS International Partnership Program (grant no. 172644KYSB20210011 (to Y.L.)), the CAS Strategic Priority Research Program (grant no. XDB36000000 (to C.C.)), the Chinese Academy of Medical Sciences Innovation Fund for Medical Science (grant no. CIFMS 2019-12M-5-018 (to C.C.)), the National Natural Science Foundation of Guangdong Province (grant nos. 2022A1515010549 (to Y.L.) and 2021B1212030007 (to J.S.)), the Research and Development Project in Key Areas of Guangdong Province (grant no. 2019B090917011 (to C.C.)), the Shenzhen Science and Technology Program (grant nos. GJHZ20190821155803877 (to Y.L.) and JCYJ20210324120200001 (to H.L.)), the Research and Development Project in Key Areas of Guangzhou (grant no. 202008070007 (to C.C.)), the Science and Technology Innovation Project of IHEP (grant no. E25459U210 (to L.W.)), the CAS President's International Fellowship Initiative (grant nos. 2022VBA0008 and 2021PB0060 (to Y.L.), and 2021PM0059 (to L.W.)), the Beijing Municipal Health Commission (grant no. 2021-1G-1191 (to L.W.)) and the State Key Laboratory of Natural and Biomimetic Drugs, Peking University (grant no. K202001 (to L.W.)).

Author contributions

Y.L., L.W. and C.C. conceived, designed and supervised the study. G.Z. and G.C. performed the biology and biochemistry experiments. H.L., X.S. and K.L. validated the pseudovirus systems. F.-L.L. and Y.-T.Z. contributed to the SARS-CoV-2 experiments in vivo. S.L. and Y.F. contributed to the organoid experiments. L.L., J.S., R.-H.L., X.-Y.L. and J.Q. performed SARS-CoV-2 experiments in vitro in the P3 laboratory. G.Z. performed the pathological analysis of the H&E images. Y.C., L.W., J.W. and Y.-F.L. performed the BLI, CD, Nano-CT, XRF and XAFS experiments. Y.C. performed chemical activity characterization of ions and CIPS. W.X. analysed EXAFS data. G.Z., G.C., Y.C., W.Y., B.L. and D. Baimanov conducted the ICP-MS experiments. L.W. and Y.C. took part in the MD simulations. F.W., L.Z., M.H., S.F. and L.W. performed MS and data analysis. P.Y. and J.Z. prepared and characterized CIPS. G.Z., G.C., W.Y. and Q.S. performed the in vivo safety experiments. Q.S., G.W. and X.-F.Y. contributed to the synthesis and characterization of nanomaterials. Y.L., L.W., C.C., H.L., D. Boraschi, Y.-T.Z., G.Z., L.F., H.W., F.-L.L. and Y.-Z.C. analysed and discussed the data. Y.L., L.W., C.C., D. Boraschi and G.Z. wrote the manuscript.

Competing interests

The authors declare no competing interests.

Additional information

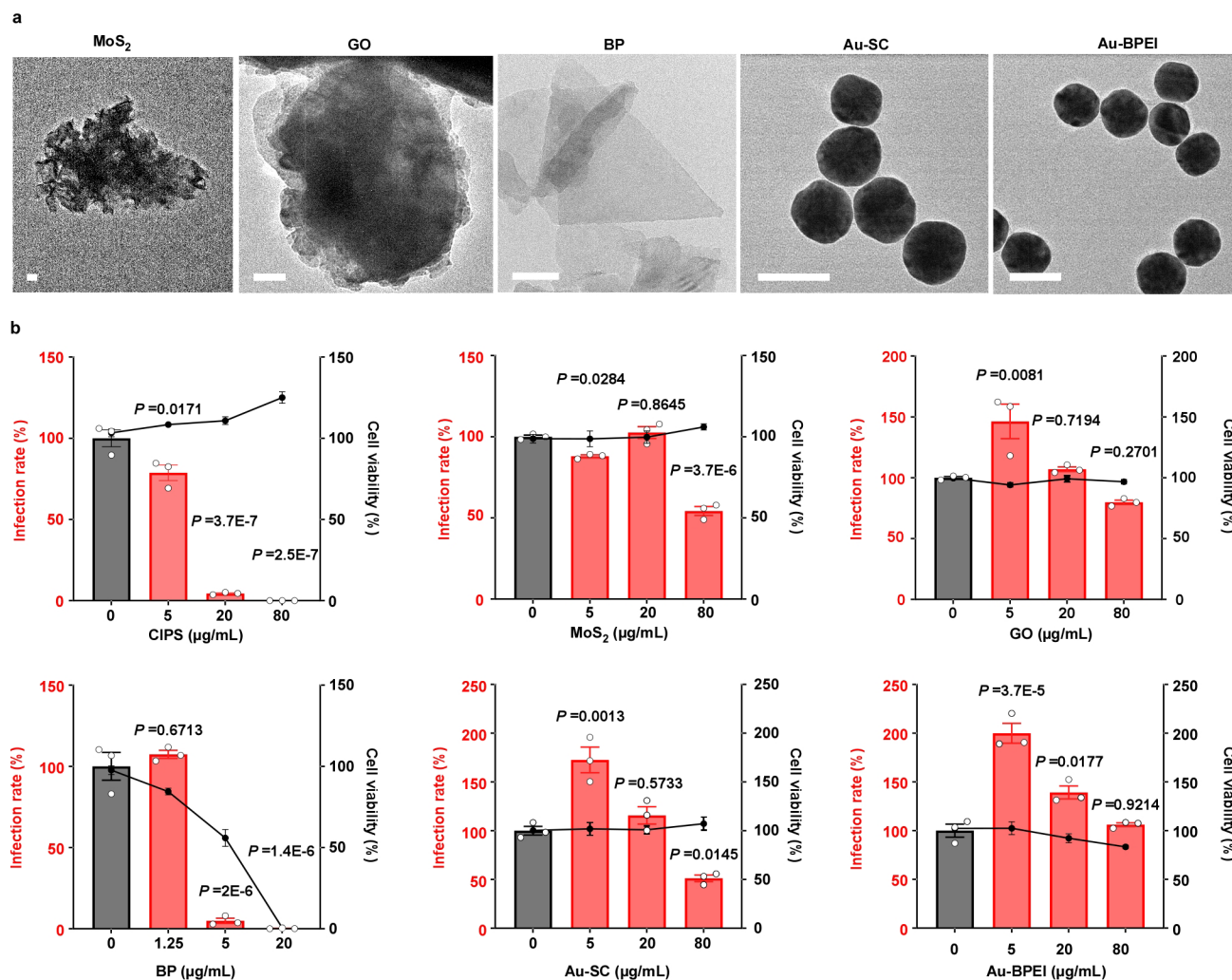
Extended data is available for this paper at <https://doi.org/10.1038/s41565-022-01177-2>.

Supplementary information The online version contains supplementary material available at <https://doi.org/10.1038/s41565-022-01177-2>.

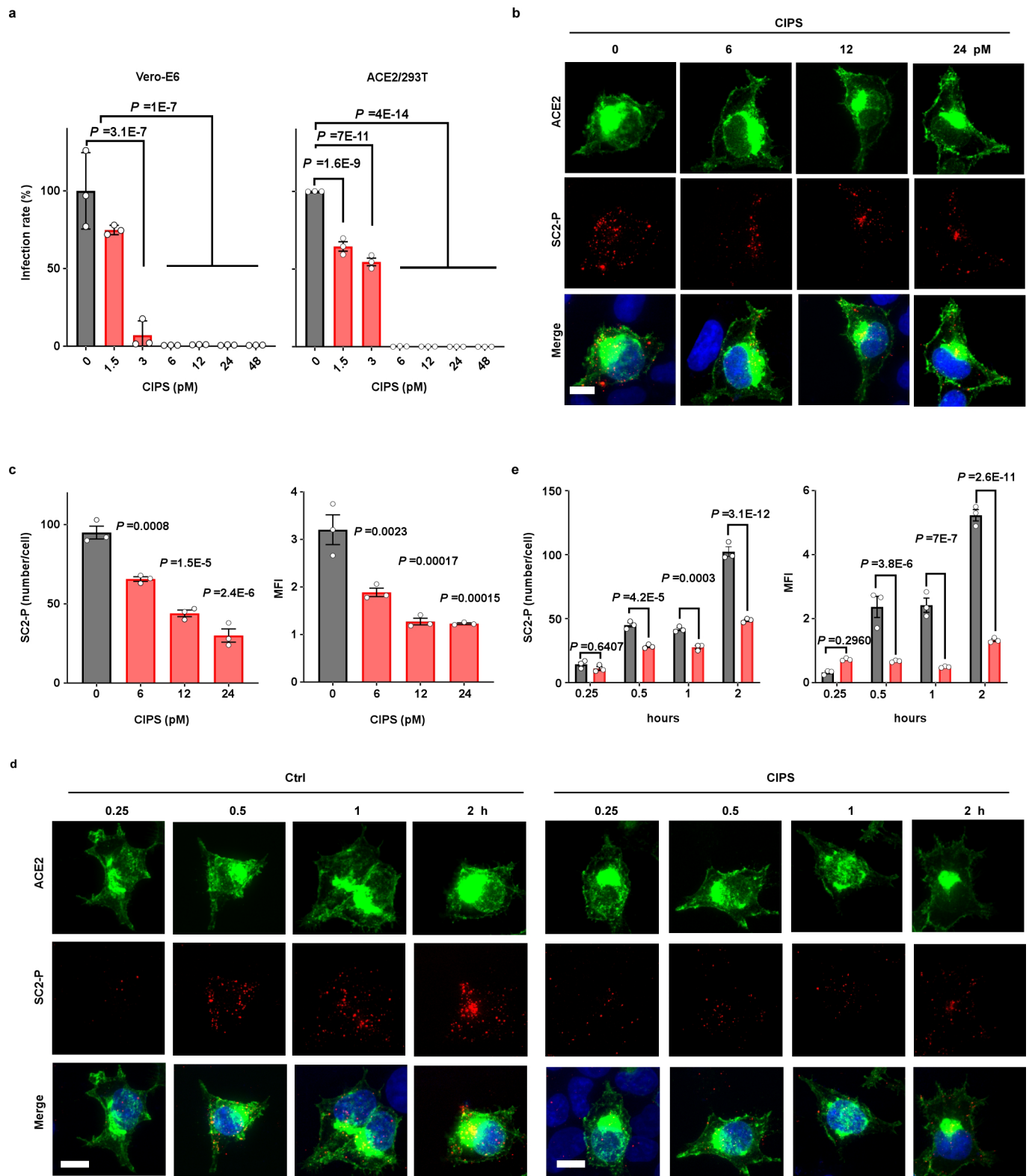
Correspondence and requests for materials should be addressed to Yong-Tang Zheng, Hongchang Li, Chunying Chen, Liming Wang or Yang Li.

Peer review information *Nature Nanotechnology* thanks the anonymous reviewers for their contribution to the peer review of this work.

Reprints and permissions information is available at www.nature.com/reprints.



Extended Data Fig. 1 | Screening of nanomaterials for potential inhibition of SARS-CoV-2 infection. a) TEM images of the examined NMs. Scale bar = 50 nm. b) The effect of NMs on the infection rate (red) and cell viability (black) of ACE2/293 T cells infected with SC2-P. LUC-containing SC2-P pre-incubated with different NMs was used for infecting ACE2/293 T cells. Infection was evaluated on cell lysates as SC2-P dependent luciferase activity after 40 h, while the percentage of metabolically active viable cells was evaluated with the CCK8 assay after exposure to NM for 48 h. Results are presented as mean \pm SEM of $n=3-5$ biological replicates. Statistical significance was calculated by one-way ANOVA with Tukey's multiple comparisons test.

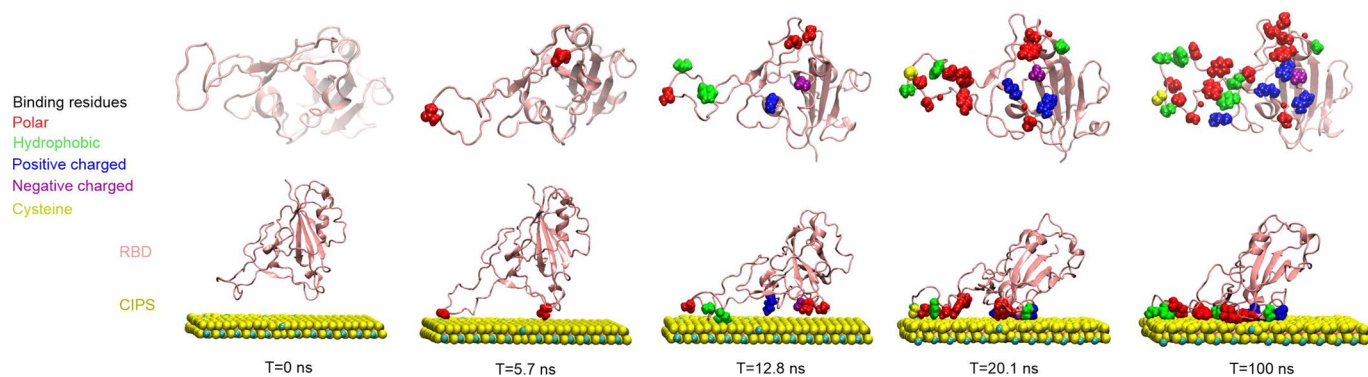


Extended Data Fig. 2 | See next page for caption.

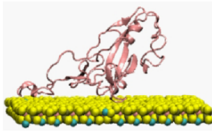
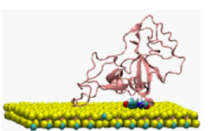
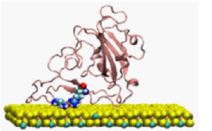
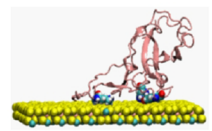
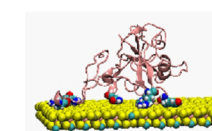
Extended Data Fig. 2 | CIPS inhibits cell infection by the SARS-CoV-2 pseudovirus SC2-P. a) The inhibitory effect of CIPS on SC2-P infection in Vero-E6 and ACE2/293T cells. SC2-P was pre-incubated with 0–48 pM CIPS for 2 h and added to Vero-E6 or ACE2/293T cells for 2 h, then washed off. Infection was evaluated after 40 h on cell lysates as SC2-P dependent luciferase activity. Data are representative of $n = 3$ independent experiments, and presented as mean \pm SEM of $n = 3$ biological replicates. b–e) Dose-dependency (b, c) and time course (d, e) of the inhibitory effect of CIPS on SC2-P infection of ACE2-OE cells. SC2-P was pre-incubated with CIPS for 2 h and added to ACE2-OE cells for 2 h (b) or pre-incubated with 12 pM CIPS for 2 h, and added to ACE2-OE cells for different times (d). Green: ACE2-GFP; red: SC2-P labeled with anti-Flag antibodies. Scale bar = 10 μm . (c, e) Quantitative and statistical analysis of IF data. The number of SC2-P within infected ACE2-OE cells was counted (left) and analyzed for mean fluorescent intensity (MFI, right). Data are from one out of three experiments performed, and presented as mean \pm SEM of $n = 3$ representative cells. Statistical significance was calculated by one-way ANOVA with Tukey's multiple comparisons test (a, c), and two-way ANOVA with Sidak's multiple comparisons test (e).

Number	Residues in RBD	Residues in ACE2	Conformational location in RBD	Interaction forces
1	LYS417*	ASP30	Turn	Salt bridge
2	TYR449	GLU37	Coil	Hydrogen bond
3	TRY453	HIS34	β -Sheet	Hydrogen bond
4	LEU455*	HIS34	Coil	Hydrophobic interaction
5	GLN474	GLN24	Coil	Hydrogen bond
6	PHE486*	MET82	Turn	Hydrophobic interaction
7	ASN487*	GLN24	Turn	Hydrogen bond
8	GLN493*	GLU35	β -Sheet	Hydrogen bond
9	GLN498*	GLN42	Turn	Hydrogen bond
10	THR500*	ARG357	Turn	Hydrogen bond
11	ASN501*	LYS353	Turn	Hydrogen bond

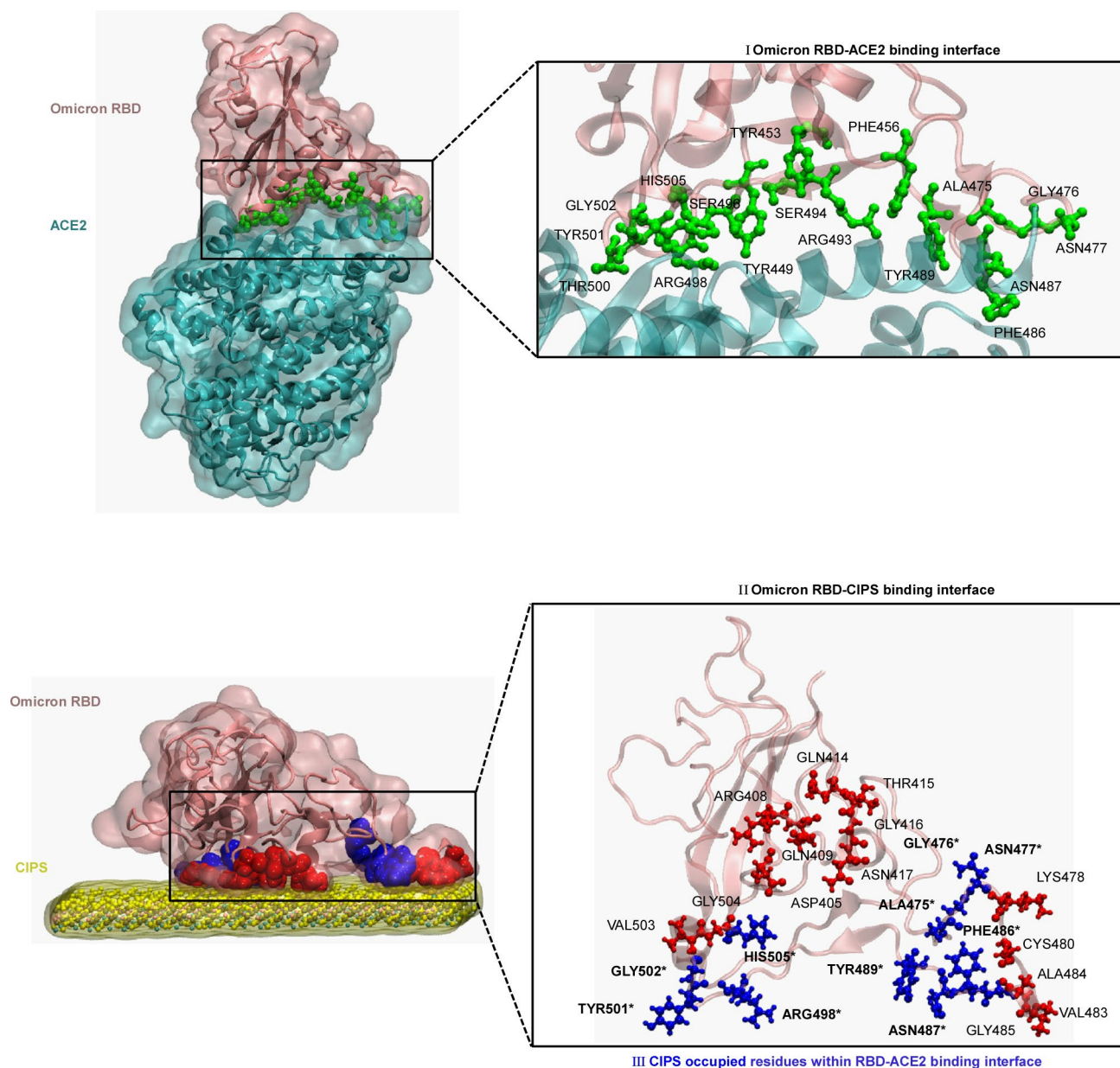
Extended Data Fig. 3 | Binding residues between RBD and ACE2. MD simulation-detected amino acid residues involved in the interaction between RBD and ACE2. In bold with * are the residues also engaged in binding to CIPS.



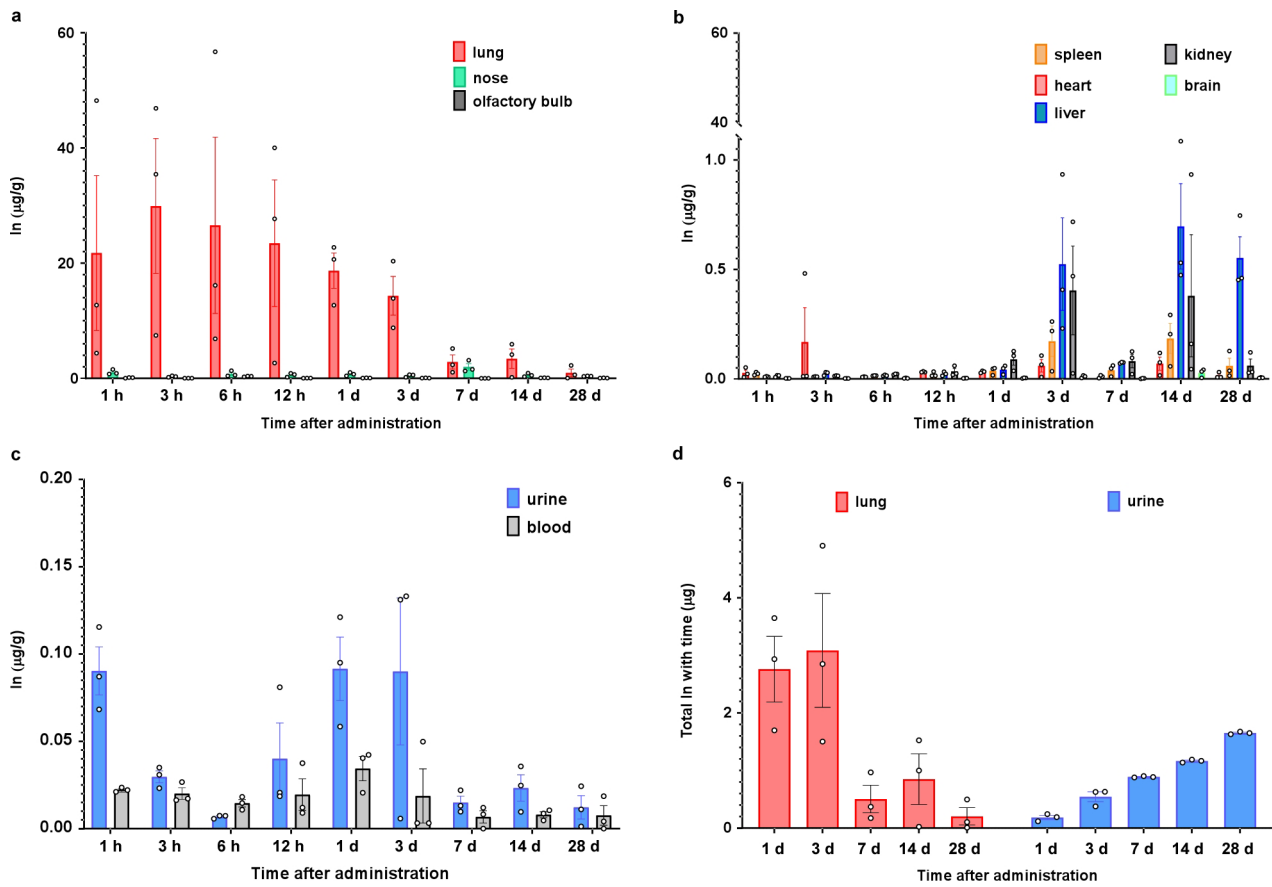
Extended Data Fig. 4 | The interaction between CIPS and RBDs. Snapshots from a representative trajectory for RBD and CIPS interaction in System 1 based on MD simulation. The time points shown below indicate the moments that the series of amino acids appear for the first time. The bottom row indicates the dynamic process of RBD adsorption on the surface of CIPS. The upper row shows the bottom view of the amino acid sites of RBD that bind with CIPS, where van der Waals spheres are the residues contacting CIPS (red, polar residues; green, hydrophobic residues; blue, positively charged residues; purple, negative residues; yellow, cysteines containing disulfide bonds).

Residue type	Cluster 1 wide type RBD	Cluster 1 RBD with 1 mutant (N501Y)	Cluster 1 RBD with 2 mutations (L452R, E484Q)	Cluster 1 RBD with 3 mutations (K417N, E484K, N501Y)	Cluster 1 Omicron RBD
Typical configurations					
-NH ₃ ⁺ (Arg, Lys, His*)	-367.84±22.34	-291.19±19.00	-61.32±30.84	-165.86±44.28	-455.44±21.52
-OH (Ser, Tyr, Thr)	-335.62±16.98	-319.13±23.53	-287.20±17.48	-357.16±83.68	-150.27±10.34
-CONH ₂ (Asn, Gln)	-155.64±8.90	-214.34±16.64	-349.54±27.02	-182.17±29.99	-196.92±17.96
-C ₆ H ₅ (Phe, Pro, Trp)	-134.35±5.81	-228.82±9.87	-191.05±17.04	-168.55±35.26	-76.20±5.47
-CH ₃ (Ile, Leu, Ala, Val)	-87.95±5.08	-102.03±5.99	-154.86±12.32	-120.96±25.99	-156.95±8.68
-H (Gly)	-124.81±3.87	-70.78±5.70	-116.34±10.23	-140.52±13.93	-150.99±7.70
-SH (Cys)	-34.59±6.49	-4.45±1.63	-15.97±6.90	-9.72 ± 2.44	-29.48±7.86
-COO ⁻ (Asp, Glu)	15.78±5.55	13.82±5.08	-0.05±0.05	1.04±1.14	-4.23±2.62
Total (kJ/mol)	-1225.04±31.14	-1216.91±38.85	-1175.33±55.67	-1143.9±205.00	-1220.49±37.09

Extended Data Fig. 5 | Binding energy of the interaction between CIPS and wild type vs. mutant RBDs. Typical interaction configurations between CIPS and wild type RBD, mutant RBD N501Y (as in VOC alpha), mutant RBD L4542R, E484Q (as in VOC delta), mutant RBD K417N, E484K, N501Y (as in VOCs beta) and omicron RBD. At 100 ns, the interaction energies and the amino acid residues mainly contributing to the binding force are shown. Compared to the interaction between CIPS and wild type RBD, the overall binding energy between CIPS and mutant RBDs does not change significantly. Data are from one representative simulation out of three performed, and presented as mean ± SD of the binding energies from 80-100 ns. The * indicates that the His only appears in the omicron RBD.



Extended Data Fig. 6 | Omicron RBD/ACE2 binding and omicron RBD/CIPS binding by MD simulation. Upper panels: MD simulation of binding of omicron RBD (pink) to ACE2 (light blue) and their binding interface (I, green) (PDB ID 7WBP). Lower panels: MD simulation of omicron RBD (pink) binding to CIPS (yellow) with indication in red and blue of the engaged RBD residues. Magnification on the right shows the residues at the binding interface (II, red and blue, measured at 100 ns in Cluster 1, presented in Supplementary Table 5), with indication of the residues overlapping with those engaged in binding to ACE2 (III, blue).



Extended Data Fig. 7 | Biodistribution and pharmacokinetics of CIPS in mice. C57BL/6J mice were administered i.n. with CIPS (8 mg/kg), and the element content of In within tissues was assessed by ICP-MS at different time points from 1 h to 28 d. a-b) In concentration in different tissues. c) In concentration in urine and blood. d) Total time-accumulated amount of In in the lung and urine, calculated based on the data from a and c. Results are presented as mean \pm SEM of $n = 3$ mice.

Reporting Summary

Nature Portfolio wishes to improve the reproducibility of the work that we publish. This form provides structure for consistency and transparency in reporting. For further information on Nature Portfolio policies, see our [Editorial Policies](#) and the [Editorial Policy Checklist](#).

Statistics

For all statistical analyses, confirm that the following items are present in the figure legend, table legend, main text, or Methods section.

n/a Confirmed

- The exact sample size (n) for each experimental group/condition, given as a discrete number and unit of measurement
- A statement on whether measurements were taken from distinct samples or whether the same sample was measured repeatedly
- The statistical test(s) used AND whether they are one- or two-sided
Only common tests should be described solely by name; describe more complex techniques in the Methods section.
- A description of all covariates tested
- A description of any assumptions or corrections, such as tests of normality and adjustment for multiple comparisons
- A full description of the statistical parameters including central tendency (e.g. means) or other basic estimates (e.g. regression coefficient) AND variation (e.g. standard deviation) or associated estimates of uncertainty (e.g. confidence intervals)
- For null hypothesis testing, the test statistic (e.g. F , t , r) with confidence intervals, effect sizes, degrees of freedom and P value noted
Give P values as exact values whenever suitable.
- For Bayesian analysis, information on the choice of priors and Markov chain Monte Carlo settings
- For hierarchical and complex designs, identification of the appropriate level for tests and full reporting of outcomes
- Estimates of effect sizes (e.g. Cohen's d , Pearson's r), indicating how they were calculated

Our web collection on [statistics for biologists](#) contains articles on many of the points above.

Software and code

Policy information about [availability of computer code](#)

Data collection

1. The amounts of Cu and In in cells, blood and organs were quantified with ICP-MS (Thermo-X7, USA).
2. Nano-CT images were captured with cryo-soft X-ray transmission microscope (TXM) (nano-CT) at the beamline BL07W of the National Synchrotron Radiation Laboratory (NSRL, Hefei, China).
3. The fluorescence spectra were measured with a fluorescence spectrometer (Hitachi F-7000, Japan).
4. The UV-Vis spectra and absorbance were measured with a PerkinElmer EnSpire Multimode Plate Reader (USA).
5. Evaluation of binding affinity were measured with the Octet RED96e system (BLI, FortéBio, Bohemia, NY, USA).
6. Secondary structure of proteins were was measured by Circular Dichroism (J-810, JASCO International Co. Ltd., Tokyo, Japan).
7. The immunofluorescence was observed by Leica MM AF v1.7 (Wetzlar, Germany).
8. The Western Bolting images were acquired by Amersham Imager 600 operation software v1.0 (GE Healthcare, USA).
9. In molecular dynamics simulation, MK-RESP (Merz-Kollman Restrained Electrostatic Potential) methodology using the Multiwfn code, the Parrinello-Rahman algorithm, the particle mesh Ewald (PME) method, the SETTLE algorithm and the LINCS algorithm, the Parrinello-Rahman method, the GROMACS software package (version 5.1.5) were used.
10. The real-time PCR experient was performed on an Applied Biosystems ABI 7500 PCR system.
11. The hydrodynamic size and zeta potential were determined by dynamic light scattering (Zetasizer Nano ZS, Malvern Instrument, UK).
12. TEM images were obtained with a Tecnai G2 F20 U-TWIN imaging system (FEI Company, USA).
13. AFM images were captured by Bruker Dimension Edge imaging system (Bruker Company, Germany).
14. The synchrotron radiation X-ray fluorescence (SRXRF) signals were collected with a Si (Li) detector. The fluorescence intensities of the elements and Compton scattering were recorded and analyzed by 8 single channel analyzers (Ortec 550) at beamline 15U1 in the Shanghai Synchrotron Radiation Facility.
15. The XANES spectra were recorded with the specific detectors in Beijing and Shanghai Synchrotron Radiation Facility.
16. The alanine transaminase (ALT) and aspartate transaminase (AST) in the serum were measured with an automatic biochemical blood analyzer (Hitachi 7100, Japan).

Data analysis

1. 3D Nano-CT was processed with Amira 5.3.1 (FEI, USA) software.
2. BLI data were analyzed with the Data Analysis 11.0 Software.
3. Circular Dichroism data were processed with the CD tool software (available at <http://cdtools.cryst.bbk.ac.uk>).
4. Imaris v7.0.0 or Leica MM AF v1.7 was used for confocal image processing.
5. ImageJ v1.50i was used for image processing.
6. GraphPad Prism v8.0 was used to analyze the data.
7. GROMACS software package (version 5.1.5) was used to perform MD simulations.
8. The XANES spectra were normalized and analyzed by IFEFFIT Athena software (Center for Advanced Radiation Sources, the University of Chicago).

For manuscripts utilizing custom algorithms or software that are central to the research but not yet described in published literature, software must be made available to editors and reviewers. We strongly encourage code deposition in a community repository (e.g. GitHub). See the Nature Portfolio [guidelines for submitting code & software](#) for further information.

Data

Policy information about [availability of data](#)

All manuscripts must include a [data availability statement](#). This statement should provide the following information, where applicable:

- Accession codes, unique identifiers, or web links for publicly available datasets
- A description of any restrictions on data availability
- For clinical datasets or third party data, please ensure that the statement adheres to our [policy](#)

The data that support the findings of this study are available within the paper and its Supplementary Information files, or from the corresponding author upon request.

Field-specific reporting

Please select the one below that is the best fit for your research. If you are not sure, read the appropriate sections before making your selection.

- Life sciences Behavioural & social sciences Ecological, evolutionary & environmental sciences

For a reference copy of the document with all sections, see [nature.com/documents/nr-reporting-summary-flat.pdf](https://www.nature.com/documents/nr-reporting-summary-flat.pdf)

Life sciences study design

All studies must disclose on these points even when the disclosure is negative.

Sample size

Sample size was determined on the basis of estimates from preliminary experiments and previous similar work:
 For animal experiment in the BSL3 lab, refer to Science. 371(6536). 1374-1378(2021);
 For the virus infection in vitro experiment, refer to Nature Microbiology, 5, 1439–1448 (2020);
 For the MD simulation, ICP-MS and XANES spectra, refer to Nature Nanotechnology, 16, 708–716 (2021).
 Sample size is indicated in the figure legends for each experiment. A minimum sample size of n=3 was used.

Data exclusions

No data were excluded from the analyses.

Replication

Experiments were replicated independently for at least three times with similar results.

Randomization

For all in vitro experiments, cultured cells were randomly assigned to experimental groups. For the animal study, mice were randomly allocated to each group before treatment.

Blinding

The investigator was blinded to the group allocation during data collection and analysis.

Reporting for specific materials, systems and methods

We require information from authors about some types of materials, experimental systems and methods used in many studies. Here, indicate whether each material, system or method listed is relevant to your study. If you are not sure if a list item applies to your research, read the appropriate section before selecting a response.

Materials & experimental systems

n/a	Involvement
<input type="checkbox"/>	<input checked="" type="checkbox"/> Antibodies
<input type="checkbox"/>	<input checked="" type="checkbox"/> Eukaryotic cell lines
<input checked="" type="checkbox"/>	<input type="checkbox"/> Palaeontology and archaeology
<input type="checkbox"/>	<input checked="" type="checkbox"/> Animals and other organisms
<input type="checkbox"/>	<input checked="" type="checkbox"/> Human research participants
<input checked="" type="checkbox"/>	<input type="checkbox"/> Clinical data
<input checked="" type="checkbox"/>	<input type="checkbox"/> Dual use research of concern

Methods

n/a	Involvement
<input checked="" type="checkbox"/>	<input type="checkbox"/> ChIP-seq
<input checked="" type="checkbox"/>	<input type="checkbox"/> Flow cytometry
<input checked="" type="checkbox"/>	<input type="checkbox"/> MRI-based neuroimaging

Antibodies

Antibodies used	The primary antibodies used for immunofluorescence and immunoblotting were as follows: anti-Acetyl- α -Tubulin (Lys40) mouse mAb (Cat. 6-11B-1, 1:500 for IF) and anti-MUC5AC rabbit mAb (Cat. E3O9I, 1:500 for IF) from Cell Signaling Technology, Inc. (Danvers, MA, USA), LAMP-1 (Cat. NBP2-52721; Novus Biologicals, Centennial, CO, USA, 1:500 for IF) and anti-Flag (AF0036; Beyotime Biotechnology, Shanghai, China, 1:500 for IF, 1:3000 for WB).
Validation	Quality of the antibodies used in the study was tested by manufacturer or relevant references cited on the manufacturer's website. Validation data are available on the manufacturer's website. 1. anti-Acetyl- α -Tubulin (Lys40) mouse mAb : https://www.cellsignal.cn/products/primary-antibodies/acetyl-a-tubulin-lys40-6-11b-1-mouse-mab/12152?site-search-type=Products&N=4294956287&Ntt=anti-acetyl-%CE%B1-tubulin+%28lys40%29+mouse+mab&fromPage=plp&_requestid=3371371 ; 2. anti-MUC5AC rabbit mAb (Cat. E3O9I): https://www.cellsignal.cn/products/primary-antibodies/muc5ac-e3o9i-xp-rabbit-mab/61193?site-search-type=Products&N=4294956287&Ntt=anti-muc5ac+rabbit+mab+%28cat.+e3o9i%29&fromPage=plp ; 3. anti-LAMP1: https://www.novusbio.com/products/lamp-1-cd107a-antibody-5e7_nbp2-52721 ; 4. anti-Flag: https://www.beyotime.com/product/AF0036.htm

Eukaryotic cell lines

Policy information about [cell lines](#)

Cell line source(s)	The human embryonic kidney cell line HEK293T (293T) (National Collection of Authenticated Cell Cultures, Shanghai, China), the human bronchial epithelial cell line 16HBE (Cell Bank of Peking Union Medical College, China), the human type II-like lung carcinoma cell line A549 (National Collection of Authenticated Cell Cultures, Shanghai, China), primary human adult epidermal keratinocytes (pHEK-Ad; Lonza, Basel, Switzerland) and African green monkey Vero-E6 cells (National Collection of Authenticated Cell Cultures, Shanghai, China). HEK-293T cells stably expressing ACE2-GFP were generated by lentiviral transduction with the pCDH-ACE2-GFP vector and were selected by flow cytometry. The human monocytic leukemia cell line THP-1 (Cat No. SCSP-567; National Collection of Authenticated Cell Cultures, Shanghai, China)
Authentication	Cell lines were not independently authenticated by STR. Following receipt from Type Culture Collection Committee of the Chinese Academy of Science, the identity of the cell lines is confirmed through assessment of cellular morphology under microscope.
Mycoplasma contamination	The cell lines were tested negative for mycoplasma contamination.
Commonly misidentified lines (See ICLAC register)	No commonly misidentified cell lines were used.

Animals and other organisms

Policy information about [studies involving animals](#); [ARRIVE guidelines](#) recommended for reporting animal research

Laboratory animals	Male 6-8 week-old mice transgenic for human ACE2 (hACE2 mice) were purchased from the Gempharmatech. Co. Ltd (B6JGpt-Ace2em1Cin(hACE2-stop)/Gpt, Cat. T037630; Nanjing, China). Six to eight weeks old male C57BL/6J mice were purchased from the Gempharmatech Co. Ltd. (Nanjing, China). The animals were housed on a standard diet and water and under animal biosafety level 3 (ABSL-3) facility or SPF conditions with an ambient temperature of $24 \pm 2^\circ\text{C}$, air humidity of 40-70% and a 12h dark/12h light cycle.
Wild animals	This study did not involve wild animals.
Field-collected samples	This study did not involve field-collected samples.
Ethics oversight	All animal experiment protocols were approved by the Institutional Animal Care and Use Committee of Shenzhen Institute of Advanced Technologies, Chinese Academy of Sciences and Institutional Animal Care or Use Committees of Kunming Institute of Zoology, Chinese Academy of Sciences.

Note that full information on the approval of the study protocol must also be provided in the manuscript.

Human research participants

Policy information about [studies involving human research participants](#)

Population characteristics	The tissues were medical waste of septoplasty, from male or female of Chinese at age of 18-70 years old. The volunteers did not have pulmonary tuberculosis, and are free from sterols and antibiotics at last three month. The tests of bacterial or fungal infection, and respiratory viruses infection, e.g. influenza virus, coronavirus, were negative. Blood tests showed no immune response to infection.
Recruitment	The participants of this study were recruited randomly. The tissues were collected by the medical doctor and given to us following the above criterion. No potential self-selection bias or other biases were present in this study could impact the results.
Ethics oversight	All the human tissue-related work was approved by the ethics committee of the Seventh Affiliated Hospital of Sun Yat-sen University, Shenzhen (No. 0720) and the ethics committee of Shenzhen Institute of Advanced Technology, Chinese Academy of Sciences (SIAT-IRB-200215-H0415)

Note that full information on the approval of the study protocol must also be provided in the manuscript.